

UC Santa Cruz

UC Santa Cruz Electronic Theses and Dissertations

Title

Electro-Plasmonic Brain-Machine Interfaces

Permalink

<https://escholarship.org/uc/item/55p380zq>

Author

Hardy, Neil

Publication Date

2022

Copyright Information

This work is made available under the terms of a Creative Commons Attribution-ShareAlike License, available at <https://creativecommons.org/licenses/by-sa/4.0/>

Peer reviewed|Thesis/dissertation

UNIVERSITY OF CALIFORNIA
SANTA CRUZ

ELECTRO-PLASMONIC BRAIN-MACHINE INTERFACES

A dissertation submitted in partial satisfaction
of the requirements for the degree of

DOCTOR OF PHILOSOPHY

in

ELECTRICAL AND COMPUTER ENGINEERING

by

Neil R. Hardy

September 2022

The Dissertation of Neil Hardy is
approved:

Dr. Ahmet Ali Yanik, chair

Dr. Mircea Teodorescu

Dr. Nader Pourmand

Peter Biehl
Vice Provost and Dean of Graduate Studies

Copyright © by

Neil R. Hardy

2022

Table of Contents

List of Figures.....	v
Abstract.....	ix
Acknowledgements.....	xii
1. Introduction.....	1
1.1. Thesis Outline.....	5
2. A Brief Review of Brain-Machine Interfaces.....	6
2.1. Electrical BMI	9
2.1.1. Neuralink.....	11
2.1.2. Neural Dust.....	14
2.2. Optical BMI.....	16
2.2.1. Electro-optic Considerations.....	17
2.2.2. GEVI.....	18
2.2.3. Quantum Dots.....	22
2.2.4. Plasmonic	23
2.2.5. Electro-plasmonic Nanoantennas	24
2.3. Methods for Bulk Activity.....	28
2.3.1. fNIRS	28
2.3.2. fMRI.....	31
3. Electro-plasmonics for High-throughput Neural Sensing.....	36
3.1. Wireless Nanoelectrode Arrays (W-NEAs).....	39
3.1.1. W-NEA Fabrication	39
3.1.2. Optical Circuit Model.....	40
3.1.3. Simulating W-NEA Spectra.....	43
3.1.4. Simulating W-NEA Resolution.....	44
3.2. Characterizing W-NEAs.....	44
3.2.1. Measuring Sensitivity	45
3.2.2. Electro-optic characterization of W-NEA.....	48
3.2.3. Temporal Response	49
3.3. High-throughput Electrophysiology with Cardiomyocytes.....	50

3.3.1.	Results	51
3.3.2.	Cell Culturing	54
3.3.3.	Immunostaining	55
3.3.4.	SEM Images	56
3.3.5.	Image Processing	56
4.	In Vivo Sensing with Electro-plasmonics	57
4.1.	Neuro-SWARM ³	59
4.2.	Field Sensitivity	61
4.2.1.	Multisphere Mie Theory and Design	62
4.2.2.	Simulating Sensitivity with a Drude Model	63
4.2.3.	Optimizing PEDOT Thickness.....	65
4.3.	Modeling Neural Sensing	68
4.3.1.	Biological Neural Activity	68
4.3.2.	Generating Electric Field	68
4.3.3.	Comparison with Quantum Dots	69
4.4.	Utilizing a Magnetic Core.....	71
4.4.1.	Magnetothermal Stimulation.....	71
4.4.2.	Delivery and Navigation.....	73
4.5.	Discussion	75
	Bibliography	77

List of Figures

Figure 1.1. Comparing neurotechnology. **a.** A comparison of neural interfaces showing they occupy different spaces in spatiotemporal resolution as well as field of view. These are compared with a theoretical ideal brain-machine (black) that has synaptic, sub-millisecond spatiotemporal resolution and can monitor the whole brain¹³. **b.** A comparison of in vivo MEA and Neuro-SWARM³ contrasting the invasive nature of the two methods. MEAs use an array of inflammatory shanks and require a headstage while an optical BMI does not significantly alter neural tissue and is otherwise non-invasive. 3

Figure 2.1. Existing brain-machine interfaces (BMIs). **a.** Architecture of a typical BMI. **b.** Traditional Utah electrode array with a US penny for scale⁵¹. **c.** Integrated silicon ‘Neuropixel’ probes for high-density recording⁴⁷. **d.** Integrated BMI developed by Neuralink showing surgical implantation (top), the device in whole head (bottom, left), and a close-up cross-section of the implanted MEA (bottom, right). **e.** Neural Dust: An ultrasonic Brain-Machine Interface⁵² 13

Figure 2.2. GEVIs. **a.** Mechanism of GEVI sensing where shifting membrane potentials alter the protonation and consequently the fluorescence (left). GEVIs under an applied voltage exhibits a step change in fluorescence (middle). An HEK 293 cell expressing the GEVI, Arch (right)⁵⁷. **b.** Setup diagram of in vivo recordings of a genetically modified fruit fly (left) and the results of recording spontaneous activity of clock neurons (right)³⁵. **c.** Setup for simultaneous two-photon (2P) imaging and patterned illumination (left) with fluorescence recordings before and during walking (middle). Portions of traces show complex spiking and subthreshold dynamics (right)⁵⁶ 19

Figure 2.3. Issues of GEVI. **a.** Target neurons are genetically modified to express fluorescence, which is not feasible in human subjects. **b.** A GRIN lens or optical cannula can be used to observe in vivo fluorescent signals, but this requires invasive surgery. 20

Figure 2.4. Quantum Dots. **a.** In the quantum confined Stark effect, electric fields applied to QDs shift the wavefunctions of charge carriers and consequently affect the photoluminescence of the QD (left). Applied electric fields quench and redshift QD photoluminescence (middle) and it’s ideal for QDs to nestle within the plasma membrane to experience the highest electric field (right)³⁶. **b.** QD-peptide-fullerene bioconjugates anchor themselves to the plasma membrane (left) and were used in mouse cortex to detect bursting behavior (right)⁶⁵. 22

Figure 2.5. Nanoantenna loading. **a.** Different optical materials are akin to different circuit elements in an optical circuit⁶⁹. **b.** A gap nanoantenna exhibits large shifts in its scattering spectrum for different gap materials⁷⁰. **c.** A plasmonic nano-resonator acts like an LC resonator and is effectively modulated with an electrochromic

polymer load. **d.** Electro-plasmonic nanoantennas confine light below the diffraction limit to produce high intensity hot spots. **e.** The spectrum of electro-plasmonic nanoantennas blue-shifts under an applied field (red, doped) and redshifts when the field is reversed (blue, de-doped). **f.** Electro-plasmonic nanoantennas experience sub-millisecond electrochromic switching times under an applied square wave potential. 25

Figure 2.6. Electro-plasmonic biosensing. **a.** Electro-plasmonic nanoantennas show vastly greater sensitivity to electric fields over bare plasmonic nanoantennas (left). Both electro-plasmonic and bare nanoantennas were placed in a parallel plate configuration with an ITO electrode to test their sensitivity to electric field where electro-plasmonic nanoantennas show very high SSNR, especially compared to bare plasmonic nanoantennas. **b.** Cardiomyocytes were cultured on a substrate of electro-plasmonic nanoantennas (left) and their scattering signal was recorded to reveal spiking at regular intervals (right)¹⁴. **c.** SPR biosensing setup for neuronal sensing (left). The plasmonic surface will change its absorbance while under different potentials (middle), which can be used to sense action potentials (right)⁷¹. 27

Figure 2.7. NIR Imaging. **a.** Attenuation length of NIR light through biological tissue shows four windows which are good for biological imaging⁷³. **b.** Diagram of simple functional NIR spectroscopy (fNIRS) where a short and long separation channel measure light intensity received from an emitter⁷⁸. **c.** fNIRS recording of different brain regions differentiates between novice and expert surgeons⁷⁵. **d.** NIR light travels in a curved path through the brain, which is longer than the source-detector distance⁷⁹. **e.** The Kernel Flow system covering whole-head measurement⁸⁰. 30

Figure 3.1. Sequential steps to fabricate W-NEA using photolithography and electrodeposition. The final result is a periodic array of nanoelectrodes as seen by SEM. 40

Figure 3.2. Wireless Imaging System. **a.** Scanning electron microscopy image of a single CM on W-NEA. In the inset, enlarged SEM image of CM on a portion of W-NEA shows the considerable size difference between the W-NEA and electrogenic cells. **b.** FDTD simulations the W-NEA indicates strong light confinement within the 25 nm thick PEDOT layer. **c.** Effect of doping (blue curve) and de-doping (red curve) of the PEDOT layer on the transmission spectra of W-NEA. Inset shows the circuit model to explain the intensity modulation of the EOT spectrum. **d.** FDTD simulation of a 5x5 wireless nanoelectrode array demonstrating how a single nanohole operates as a wireless nanoelectrode. These are the same nanoholes as pictured in Figure 3.1b captured in the plane of the gold surface. PEDOT was doped only around the central nanohole and it exhibited increased light transmission and field confinement compared to fully de-doped nanoholes, whereas surrounding nanoholes did not. 43

Figure 3.3. Electrochromic loading effect on gold nanoholes. **a.** Electric field sensitivity to the differential transmission signal for W-NEA and nanoantennae array

in 1x PBS. The inset shows the schematic of the plasmonic resonator loaded with the electrochromic polymer representing nanoantennae. **b.** Diagram comparison of darkfield imaging a nanoantennae array and brightfield imaging a W-NEA. **c.** Transmission switching of W-NEA recorded in ionic solution in three-electrode spectroelectrochemical cell. A square wave potential alternating between -500 mV and 500 mV versus Ag/AgCl was applied to the working electrode with a potentiostat. Transmitted signals through W-NEA were recorded with a spectrometer with an integration time of 10 ms. **d.** Equivalent circuit model of gold-PEDOT-electrolyte system. In this equivalent circuit, a solution resistance R_S is added in series with an electrolyte-polymer interface element consisting of an electrical double layer (non-faradic) capacitance C_{EDL} and a charge transfer resistance R_{CT} . The bulk redox capacitances of the electrochromic polymer are incorporated into this circuit in series by means of the electronic bulk capacitance C_{PEDOT} and finite-length Warburg diffusion impedance $Z_{Warburg}$, which is characterized by the diffusional pseudocapacitance C_D 46

Figure 3.4. Cellular voltage imaging potential. **a.** Experimental schematic showing key components. An LED source illuminates an electrogenic sample on a W-NEA substrate. Transient electric field during cellular firing events modulates the transmission intensity of the W-NEA and an sCMOS camera captures the result. **b.** Frames of a single cell combine to show electric field dynamics with high resolution. **c.** Optical recording of spiking from a single cell on a W-NEA. Pixels within a cell body outline were summed and filtered (see methods) to show single cell intensity changes..... 52

Figure 3.5. Large-scale, high-resolution electrophysiology. Processed images of W-NEA intensity in the full frame (2048 × 2048 pixels) in response to transient electric field during the cellular firing event of a large number of neonatal rat cardiomyocytes (CMs) with a temporal resolution of 30 ms. Red regions denote clusters of depolarizing CMs. The inset shows a heatmap of a single CM cellular firing event. 54

Figure 4.1. Mechanism of Operation. **a.** Neuro-SWARM³ enables remote detection of neural cell activity using NIR-II light far-field scattering. **b.** Cell depolarization (spiking) causes a high transient electric field leading to increased light scattering and red shifting of the electro-plasmonic (electrochromic-plasmonic) nanoantenna resonance spectrum. Return to resting potential (repolarization) results in reversal of the scattering spectrum changes..... 61

Figure 4.2. Sensitivity comparison. **a.** Optical scattering efficiency, Q_{scat} , spectra for silica-gold nanoshells loaded with PEDOT: PSS. Electric field dependence is shown for 0-12 mV/nm with increments of 4 mV/nm. A core-shell nanoparticle with 63 nm silica core radius, 5 nm thick gold shell, and 15 nm thick PEDOT: PSS coating is considered. Inset shows an equivalent “lumped” optical nanocircuit model of the

Neuro-SWARM³. Local electric-field signal (cell spiking) is translated to the nanoantenna backscattering spectrum through the capacitive (PEDOT:PSS) loading effects. **b.** Electric field dependent change in quantum dot (QD) fluorescence based on the quantum-confined Stark effect (inset). Here QDs require an electric field nearly twice as strong for the same modulation in optical response³⁶..... 65

Figure 4.3. Effects of adding an electrochromic polymer **a.** Differential scattering signal for Neuro-SWARM³ with varying PEDOT:PSS load thickness. The polar plot of the angular scattering by the nanoprobe for linearly polarized incident light (1050 nm) in the x direction is shown in the bottom left (inset). The top inset illustrates how the scattering angle is defined within the xz plane. Electromagnetic “hotspots” due to plasmonic hotspots at 1050 nm are shown in the bottom right (inset). Finite difference time domain (FDTD) calculations were employed to calculate angular scattering and cross-sectional field profile. **b.** The SSNR of Neuro-SWARM³ improves with added PEDOT thickness up to ~15 nm which matches Figure 4.3a. Notably, the sensor response is very linear regardless of electrochromic thickness. 67

Figure 4.4. Simulated electrophysiological recordings with Neuro-SWARM³ and quantum dots (QDs). A phasic spiking Izhikevich model is used for the neural spiking activity at pseudo-random times. The input and resulting membrane voltage are shown (bottom, black). Differential scattering signal detected from 10³ Neuro-SWARM³ probes (red, top) is shown assuming a light intensity of 10 mW/mm² at 1050 nm. Differential fluorescence signal obtained from 10⁵ CdSe quantum dots is compared for an illumination intensity of 100 mW/mm² (middle, blue). A maximum extracellular field of 3 mV/nm is assumed. Scales indicating the photon count for the differential signal and the standard deviation due to the shot noise are shown on the left and right, respectively. 70

Figure 4.5. A Magnetic Neuro-SWARM³. **a.** The principal mechanism of magnetothermal stimulation¹¹⁷. **b.** The result of multiphysics simulations demonstrating nearly identical thermal output. **c.** Scattering spectra of magnetic Neuro-SWARM³ particles under different applied electric fields. **d.** Summary illustration showing intracarotid delivery, magnetic navigation, and non-invasive recording. 72

List of Tables

Table 3.1. Summary of previously reported high-resolution and high-throughput field probes compared to this work. 54

ELECTRO-PLASMONIC BRAIN-MACHINE INTERFACES

Neil Hardy

Abstract

A novel high-throughput, high-resolution platform for electrophysiology is presented as the foundation of a new generation of brain-machine interfaces. Scientists and engineers have pursued large scale neural sensing for decades; however, physical limitations associated with electrical (electrode-based) field recordings hinder advances in both field of view and spatial resolution. Electrochromic plasmonics (electro-plasmonics) has recently emerged as a novel extracellular method for label-free optical electrophysiological sensing. However, initial demonstrations were limited to dark field measurements, which are not suitable for large area imaging applications. In this thesis, I report an important advancement in electro-plasmonic sensing techniques that utilizes nanohole-based devices and extraordinary light transmission effect. A bright-field configuration based electro-plasmonic nanohole arrays yields an extremely sensitive transducer of electric fields. Furthermore, these electro-plasmonic “nanoelectrodes” allow sub-millisecond temporal resolution without cross talk to neighboring nanoelectrodes as demonstrated in controlled experiments. Upon demonstrating the operation of this new configuration, the device was successfully used for large scale electrophysiological imaging of cardiomyocytes in vitro. Subsequently, I discuss electro-plasmonic nanoshell antennas as in vivo probes for detecting electrogenic cell activity in live animals with high-resolution. The sensitivity of these

devices allows diffraction-limited resolution measurement without photobleaching and phototoxicity issues that typically plague genetically incorporated fluorescence reporters.

To my parents Robert and Susan Hardy and
to my younger self

Acknowledgements

First and foremost, I would like to thank my advisor Dr. Ali Yanik. His guidance and perspective have been invaluable during my graduate studies. I thank Dr. Sasha Sher for mentoring me on my arrival to graduate school at UC Santa Cruz; I surely would not be where I am today without his support and understanding. I would also like to thank Dr. Ahsan Habib, whom I worked most closely with in my research. I thank my labmates Dr. Xiangchao Zhu, Mustafa Mutlu, Ray Jara, and Reefat Romel for their collaboration and scientific spirit. Of course, I thank my committee members Dr. Mircea Teodorescu and Dr. Nader Pourmand for reviewing my dissertation. Finally, I thank the undergraduates I mentored during my time at UCSC including Nicholas Wetherell, Tanya Ivanov, and David Petersen.

1. Introduction

Electrophysiology is an exciting field that has seen extraordinary advances since its inception in the late 18th century during the time of Galvani and Volta. Devices which interrogate the function of neurons, cardiomyocytes, and other electrically active cells are not only crucial for advancing fundamental biological understanding, but also for the development and manufacturing of life-changing therapeutics and prosthetics. There are many kinds of tools to interface with– or otherwise record– electrogenic cellular activity; the first use of a neural interface could be attributed to Leopoldo Nobili who was the first to record neural activity in a frog neuromuscular preparation with an electromagnetic galvanometer in 1828¹. However, in this dissertation I will be focusing on advances from the late 20th century to present day. Recently, there have been numerous efforts to advance electrical, optical, and other technologies to increase resolution and field of view in electrophysiological measurements.

Microelectrode arrays (MEAs) are the workhorses of many modern electrophysiology labs and have seen significant advances over the past few decades. MEAs allow for the monitoring of neural activity on a network scale by measuring extracellular potentials. Scientists began using MEAs in the 1950's, but it wasn't until the introduction of chip-based fabrication in the late 1970's that scientists first developed the MEA for in vitro recordings². After decades of improvement and research, MEAs became recognized as a powerful tool for rapidly testing many pharmacological compounds and saw widespread use in drug screening and

neurotoxicity testing by the 2000's^{3,4}. Breakthroughs in silicon electronics continued to improve MEAs with the emergence of complementary metal-oxide semiconductor (CMOS) technology, which was used to make the first high-density (HD-)MEAs in the turn of the 21st century. MEAs integrated CMOS amplifiers and filters at the site of the recording electrode to boost MEA resolution (30 μm to $\sim 10 \mu\text{m}$)⁵. However, at this resolution, MEAs encounter physical limitations in spatial resolution and electrode count. Crosstalk between electrodes and the required footprint for CMOS electronics renders higher electrode density impractical. The footprint taken up by CMOS electronics also crowds electrode routing and prevents further scaling in area while maintaining high-density resolution⁶.

Genetically encoded voltage indicators (GEVIs) have recently attracted considerable attention as a voltage-sensitive fluorescent probe for electrophysiology^{7,8}. Engineered viruses can target neurons to express a voltage-sensitive fluorescent protein on its surface. Gradual biochemical improvements have been made since the first GEVI was made in 1997⁹ to increase the sensitivity of these reporters such that populations of neurons can be monitored with optical resolution¹⁰. GEVIs have been shown to be able to resolve synaptic activity on rare occasion, but with great difficulty¹¹. The dominant issue with GEVI is cross-section and ultimately photon count, which severely limits the signal-to-noise ratio (SNR) of the probe and hence its monitoring abilities¹².

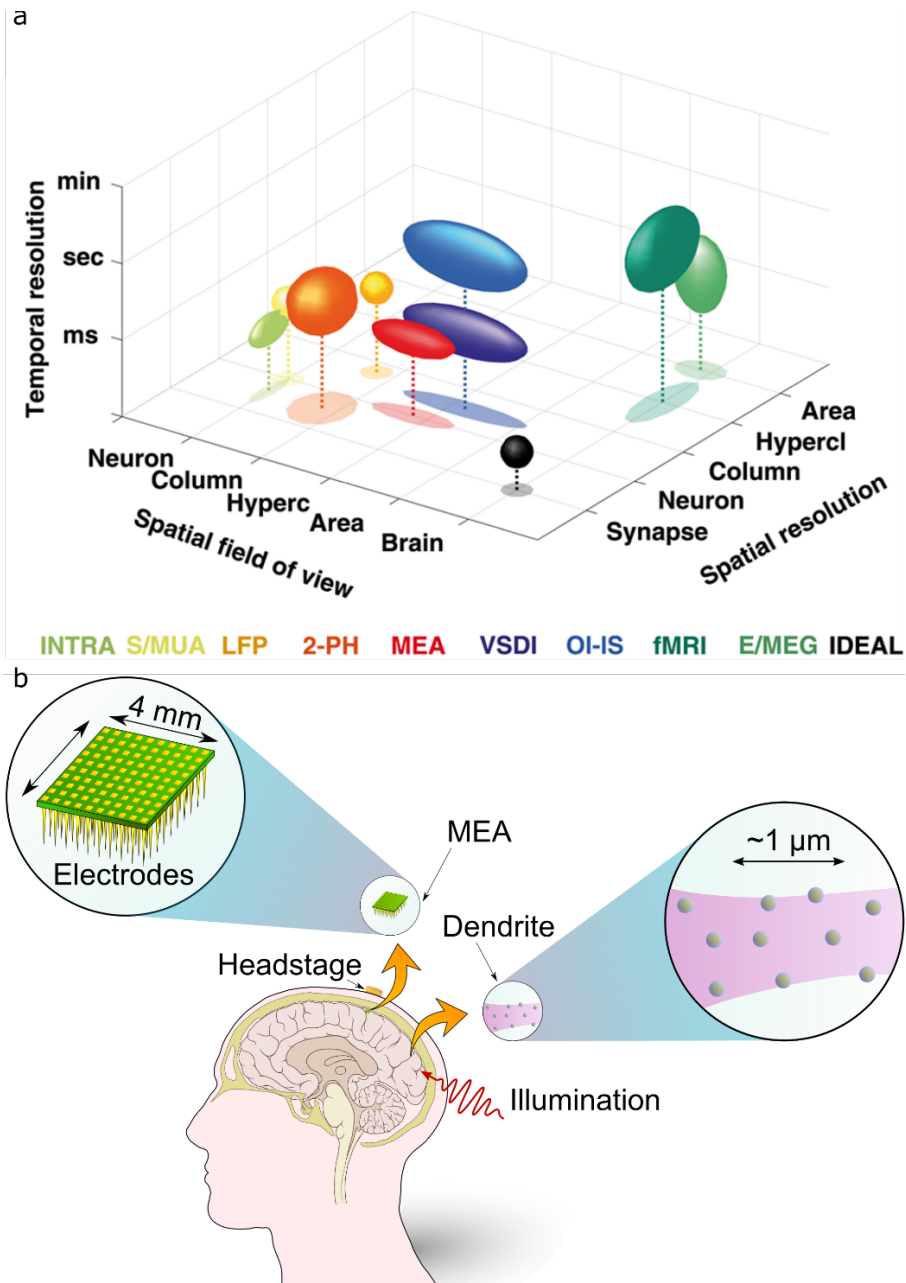


Figure 1.1. Comparing neurotechnology. **a.** A comparison of neural interfaces showing they occupy different spaces in spatiotemporal resolution as well as field of view. These are compared with a theoretical ideal brain-machine (black) that has synaptic, sub-millisecond spatiotemporal resolution and can monitor the whole brain¹³. **b.** A comparison of in vivo MEA and Neuro-SWARM³ contrasting the invasive nature of the two methods. MEAs use an array of inflammatory shanks and require a headstage while an optical BMI does not significantly alter neural tissue and is otherwise non-invasive.

Many technologies occupy a spatiotemporal niche in neuroscience, and developers are constantly moving toward a more ideal neural interface. The ideal method must realize neural activity monitoring with synaptic spatial resolution and sub-millisecond temporal resolution. The perfect method would also be able to survey the entire brain. There has yet to be a widespread technology which can monitor an area (2 x 2 mm) with subcellular or even single-cell resolution (Figure 1.1a), and many strategies are needed to accommodate different scales of interest¹³. However, within the last few years a new physical mode to transduce neural activity has been introduced to overcome these technological barriers.

A new technique combining electrochromic materials and plasmonics (electro-plasmonics) pioneered by Habib et al.¹⁴ was recently developed as a new physical transduction mechanism of electrophysiological activity. A periodic array of plasmonic nanoantennas were selectively coated in electrochromic polymer via electrodeposition. Using dark-field microscopy, they were able to record the extracellular spiking activity of neurons cultured on these field sensors. However, despite showing high signal-to-shot-noise (SSNR) measurement capability, dark field spectral measurements employed to collect optical signal from electro-plasmonic nanoantenna are not amenable for large area recordings.

In this dissertation, I present a new electro-plasmonic configuration enabling bright-field measurements through nanohole-based devices with extraordinary light transmission effect. This new configuration takes advantage of bright field microscopy to boost photon throughput and achieve five times higher sensitivity than previous

electro-plasmonic sensors due to increased sensitivity of nanohole devices with respect to plasmonic nanoantenna. Such advances are grounds for a new generation of brain-machine interfaces (BMIs), and I describe the mechanism, experimental design, and results in the final Chapter of this thesis. Beforehand, I present a limited review of literature on existing BMIs to provide context for this new method. I discuss electrical methods with a focus on microelectrode implementations, optical methods including electro-plasmonics, and BMI that interrogate bulk hemodynamic properties to track brain activity.

Finally, I demonstrate another technology to implement electro-plasmonic neural sensing *in vivo* to form the basis for a human BMI. This implementation of electro-plasmonic sensing is meant to be delivered to the brain through the blood-brain barrier with an intracarotid injection. It is minimally invasive as it presents the opportunity for transcranial voltage recording, especially compared to conventional electrical BMI (Figure 1.1b). I compare the performance of these new sensors to up-and-coming BMI candidates, quantum dots, and explain the significantly enhanced SSNR of electro-plasmonic sensors. Lastly, I discuss considerations for crossing the blood-brain barrier, how to transform these sensors into a truly bidirectional BMI with magnetism, and end with closing statements.

1.1. Thesis Outline

Chapter 1: Introduction. In this chapter, I present a brief background on neural sensors including electrical and optical devices and outline this thesis.

Chapter 2: A Brief Review of Brain-Machine Interfaces provides a limited review of current brain-machine interfaces. I describe electrical, optical, and bulk BMIs, including prior development in electro-plasmonic sensing.

Chapter 3: Electro-plasmonics for High-throughput Neural Sensing describes the operation, experimental design, and results of a new electro-plasmonic configuration. I show how this greatly improved sensor can be used for high-throughput neural sensing.

Chapter 4: In Vivo Sensing with Electro-plasmonics. Here, I describe the design and simulated performance of a novel in vivo electro-plasmonic probe. This device can form the basis of a new human BMI, its performance compared to other optical BMIs, and how it can be made into a bidirectional BMI by introducing magnetic materials.

2. A Brief Review of Brain-Machine Interfaces

Brain-machine interfaces are direct functional interfaces between neurons or neural tissue and artificial devices that allow brain activities to control external devices or even computers¹⁵⁻¹⁷. BMIs collect, evaluate, and interpret brain signals into commands that are delivered to an output device to perform a desired action¹⁸. There are many kinds of BMIs including electrical, optical, and bulk measurement BMIs; this is not an exhaustive review, and notably electroencephalography/electromyography (EEG/EMG)¹⁹ and single electrode interfaces (namely deep brain stimulation)²⁰ are not included. Here I review prevalent BMIs such as in vivo MEAs, fluorescent reporters, whole brain techniques, and briefly electro-plasmonic interfaces.

Intracortical MEAs are typically implanted chronically in the cerebral cortex for the measurement of brain signals or signal acquisition. The majority of intracortical MEAs are based on the seminal Utah Array, a small chip the size of Lincoln's face when placed on a penny²¹. The Utah Electrode Array is currently the only one approved by the food and drug administration (FDA) for implantation in humans²². It is a collection of microscopic shanks pressed into the brain, which causes an immune response, the formation of glial scars, and requires careful invasive surgery to be implanted^{15,23,24}. This is exactly the technology that the ever-popular Neuralink is developing for their brain-machine interface. It's a few thousand electrodes gathering non-cell-specific spikes from a small region of the brain. Neuralink has developed 'Link,' a sealed, implanted device that processes, stimulates, and transmits neural signals. It employs flexible threads for electrode containment, an inductive wireless charger to charge the implant from the outside, and a robot surgeon to place electrodes into the brain. However, Neuralink does not offer a fundamentally new capability with respect to other MEAs. As a result, the limitations of MEAs remain as they have the last several decades. Assume we have a solution with the following characteristics: (1) it enables direct read-out through the skull, (2) it avoids invasive surgical procedures; it enables wireless excitation and remote detection, so it does not require wiring or power supply, (3) it can be delivered to different regions of the brain without surgical operations, (4) it eliminates the need for front-end signal processing, and it opens the door to large scale in vivo measurements that are not limited by electrode dimensions, physical wiring, and electronic bandwidth limitations, (5) it is much smaller than the

critical dimensions that trigger glial cell response ($\sim 12 \mu\text{m}$)²⁵; it offers a long term operation capability. Creating a probe that incorporates these five fundamental advancements could be transformative for BMI research.

Due to the development of increasingly powerful electro-optic probes, optical imaging has lately surpassed electrophysiology in terms of neural yield²⁶. Recent advances have increased the number of cells simultaneously recorded in the mouse brain to one million, almost a tenth of its cortex, owing to remarkable spatiotemporal resolution measurements powered by photons²⁷. Optical electrophysiology technologies such as genetically encoded voltage indicators (GEVIs) have recently attracted considerable interest²⁸⁻³⁰. GEVIs, which are based on fusions of a fluorescent protein to a voltage-sensing domain, provide a strong optical response to membrane potential changes³¹. However, due to the small cross-sections of molecules ($\sim 10^{-2} \text{ nm}^2$)³² and quantum yields ($\sim 10^{-3}$ to 10^{-2})³³, fluorescence-based bioelectrical measurements suffer from poor signal-to-noise ratio limitations³⁴. Moreover, GEVIs require invasive genetic modifications³⁵. Field-sensitive quantum dots (QDs) have emerged as extracellular alternatives to GEVI, circumventing the need for genetic mutations³⁶. QD field probes have relatively larger much larger cross-sections ($\sim 1 \text{ nm}^2$)³⁷ than GEVI. However, QDs use the quantum confined stark effect (QCSE) for electric field detection, a relatively weak effect. Hence, QD field-probes suffer from shot-noise limitation much like GEVIs, but instead due to an electric field sensitivity issue.

In this chapter, I present a review up to the very recent research advances on brain-machine interfaces, covering thoroughly the field of electrode and optical technology. Subsequently, I go beyond that to highlight prospective research directions toward in vivo neurophotonics and identify the emerging research challenges. It is organized as follows: sections 2.1 and 2.2 discuss existing brain-machine interfaces, namely electrical and optical technologies, respectively. Amongst the various electrical approaches employed to construct BMIs, the focus is mostly on Neuralink and Neural dust as these approaches are already advanced among other electrode-based approaches. I also review the recent evolution of our understanding of the mechanisms of electro-optic translation of electrophysiological activity, focusing on fundamental parameters that have yielded new insights and questions about the optical transduction of local field dynamics. Next, in Section 2.2, I also discuss previously developed electro-plasmonic techniques where small extracellular fields generated by spiking electrogenic cells can lead to optically measurable changes in the electrochromic material. Finally, in Section 2.3, I discuss the measurement of bulk effects for monitoring brain activity.

2.1. Electrical BMI

The number of BMI tools available for recording neural signals from the brain has increased due to technological advances in physics, neuroscience, and engineering. Since Jacques Vidal's early proposal in the 1970s, Utah Arrays utilizing electrical recordings have shown tremendous potential for BMI because of their high resolution and signal-to-noise ratio¹⁷. Optical BMIs have also generated a great deal of interest

because light provides unparalleled (wavelength/time/space division) multiplexing and information carrying capabilities³⁸. For the evaluation of BMI technologies most impactful characteristics are the following: i) small size to limit the impact of scarring; ii) wireless communication between the neural sensor node and the control node outside the skull; to enable nodes to be truly free-floating, to avoid infections; iii) the neural sensor is self-contained from an energy perspective; iv) lifetime; the physical substrate in the front end should be able to withstand a wide range of biotic and abiotic effects; v) noninvasive brain implantation; preferably via injection^{23,39,40}.

To achieve a high resolution BMI, neural recording via direct electrical measurement of potential changes near relevant neurons via conducting electrodes is used^{40,41}. The generic representation of an electrode-based BMI is shown in Figure 2.1a. Almost every recording system developed to date incorporates this architecture. The potential relative to a reference electrode is recorded using a neighborhood electrode or multiple electrodes⁴⁰. Following signal extraction, it is digitalized and transmitted to the decoder node located outside the skull via a wired or wireless link. The decoder node is then connected wirelessly or via wire to the translational unit.

In electronic BMIs, substrate integrated MEAs have been the workhorse of electrophysiology laboratories for decades^{42,43}. MEAs detect electrical potential changes in the extracellular space caused by membrane current; a higher potential indicates a higher membrane current²⁸. In vitro and in vivo MEA neural interfaces are widely used in neuronal signal detection, and because their functionalities overlap significantly, in vitro neural interface concerns provide the basis for in vivo brain-

machine interface challenges⁴⁴. Most in vivo MEAs are based on the seminal Utah array, which is an array of microscopic shanks that are surgically implanted into the brain (Figure 2.1b). The Utah Array has a 10-by-10 matrix arrangement of 100 recording sites connected to external amplifiers and filtering⁴⁵. The old Utah Array technology has two limitations as a BMI technology: (i) the number of recording sites and (ii) the formation of glial scars around the electrodes. To gain a better understanding of the brain's coordinated activity, it is critical to increase the number of neurons that can be recorded concurrently by increasing the density of recording sites on a probe. Numerous voltage-recording microelectrode array devices including some commercial products like 'MicroProbes', 'NeuroNexus', 'Neuropixels', etc. have been developed with improved electrode densities (Figure 2.1c)^{43,46,47}. On the other hand, the second issue arises because the elastic modulus of the probes is significantly greater than that of neural tissues, resulting in the creation of glial scars around the electrodes that eventually encapsulate (insulate) the electrodes⁴⁸. This complication limits recordings using chronically implanted MEAs to a typical operation time of a few years or less due to the decrease in SNR⁴⁹.

2.1.1. Neuralink

Due to the wire connections between the wearable 'acquisition unit' and the 'translation unit', conventional BMI systems have limited portability and wearability⁵⁰. Neuralink presented a wireless, high-channel-count brain-machine interface (BMI) recently. The acquisition unit is a conductive coil hidden behind the ear that is implanted into the brain via micron-scale threads that include thousands of electrodes

for the detection of neural signals and activities (Figure 2.1d). The coil wirelessly connects to a wearable translational unit called 'Link' via the skin. In addition, Neuralink has created flexible electrode threads, which is less invasive than the traditional Utah Array technology.

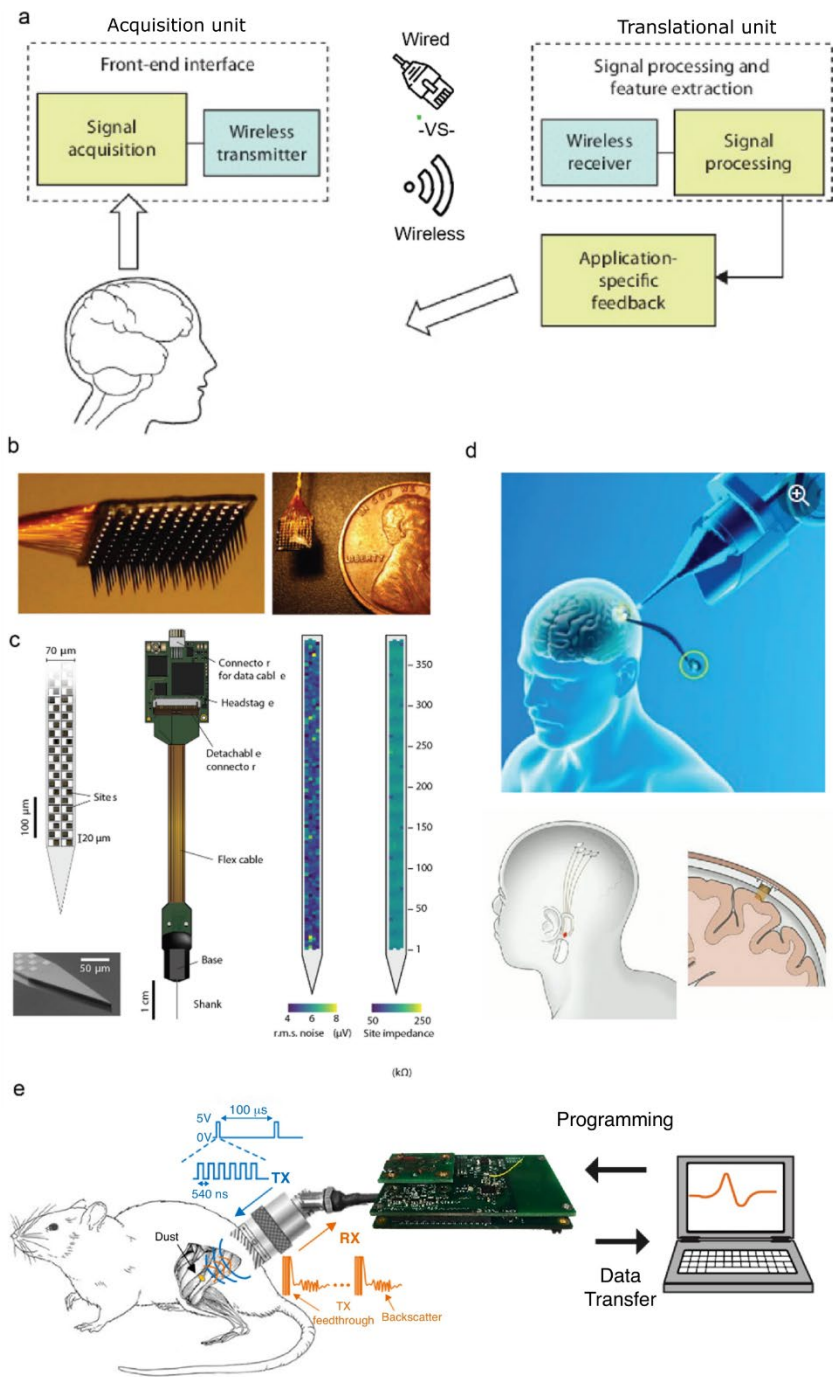


Figure 2.1. Existing brain-machine interfaces (BMIs). **a.** Architecture of a typical BMI. **b.** Traditional Utah electrode array with a US penny for scale⁵¹. **c.** Integrated silicon ‘Neuropixel’ probes for high-density recording⁴⁷. **d.** Integrated BMI developed by Neuralink showing surgical implantation (top), the device in whole head (bottom, left), and a close-up cross-section of the implanted MEA (bottom, right). **e.** Neural Dust: An ultrasonic Brain-Machine Interface⁵².

The threads are 4 to 6 μm in width, substantially thinner than a human hair, and each array has up to 3,072 electrodes distributed across 96 threads– a considerable improvement in the multiplexing capability over the Utah Array.

Although Neuralink's brain interface system is cutting-edge, it still leaves some extremely difficult problems unsolved. To begin, Neuralink's demonstration is still missing a wireless transmitter: It requires a wired connection between the acquisition unit (i.e., conductive coil) and the threads inside the brain, which limits the number of electrodes. Although Neuralink demonstrated over 3000 electrodes, this number may be insufficient to capture the brain signals required for a variety of applications. Additionally, because Neuralink implants are primarily reliant on wire electrodes, they can cause tissue inflammation over time. Second, the implant's longevity may be a source of contention for Neuralink. Despite the fact that Neuralink uses thin, flexible electrodes, the electrode-induced tissue damage during insertion has not been resolved. The final issue with the Neuralink system is its battery dependability. It is necessary to have a significant amount of power per channel, on the order of μW . Delivering this amount of power to a neural sensor node and maintaining it for ten years or more is difficult. The majority of battery solutions are either insufficiently long-lasting or made of materials that are not directly implantable⁴⁰.

2.1.2. Neural Dust

The use of acoustic waves to interact with neural sensors offers the advantage of higher spatial resolution and decreased attenuation in the tissue. Maharbiz et al. demonstrated the 'neural dust' platform that uses ultrasonic power and communication

to enable a wireless, and battery-free system⁵³. It consists of thousands of $\sim 50 \mu\text{m}$ thick, free-floating, independent sensor nodes, or neural dust, that detect and report local extracellular electrophysiological data and a sub-cranial interrogator that establishes power and communication links with the neural dust(Figure 2.1e)^{53,54}. Neural dust communicates via backscattering, a technique similar to that used in radio frequency identification (RFID) technology⁵³. The interrogator emits an ultrasonic pulse, which is reflected by the neural dust sensors (Figure 2.1e). The piezoelectric crystal detects the neural signal, and the ultrasonic energy reflected back to the interrogator is modulated in such a way that the recorded activity is communicated. Due to its compact size, wireless capability, and battery-free technology, neural dust is in a class of its own, giving various advantages over other recent BMI systems. The small size- 1.7 mm^3 , or approximately the size of the date on a US penny-allows for the placement of several (hundreds to thousands) sensors close together to obtain more exact recordings of nerve activity from multiple points inside a nerve or group of nerves⁵⁵. Because of their small size, they can be inserted via injection, which is more convenient, less expensive, and less invasive than surgery, minimizing the impact on surrounding tissue during insertion⁵⁵. Finally, the neural dust wirelessly connects with the control node placed outside the skull, enabling nodes to be truly free-floating and hence immune to infection.

Although neural dust offers several advantages in comparison to other state-of-the-art systems- further miniaturization may be difficult due to the power transfer efficiency drop. For a dust node with a diameter less than $100 \mu\text{m}$, the

effectiveness of ultrasonic power transfer is largely dependent on the cross-sectional area of the neural dust: it decreases quadratically with decreasing neural dust dimension⁵⁴. Another challenge in size-reduction emerges as a result of neural dust detecting biopotentials via voltage recording electrodes. Due to the differential nature of electrical potential measurements, when devices scale down and the distance between recording locations reduces, the absolute magnitude of the detected potential diminishes, resulting in increased noise⁵⁴.

2.2. Optical BMI

Powered by light's unprecedented spatiotemporal resolution capability to detect electrophysiological signals, optical electrophysiological techniques have evolved into powerful tools for shedding light on the brain's form and function³⁴. Optical techniques produce atypical detection compared to classical electrical systems: (1) optical techniques offer high spatial resolution; fundamentally light allows remote measurement with diffraction limited resolution, (2) optical techniques measure electric field, not potential drop. Hence, optical techniques are fundamentally only diffraction-limited in terms of the resolution and size of the probe. In contrast, for MEAs, the resolution of the system is defined by the reference and working electrode distance. Therefore, it is reasonable to speculate that optical electrophysiological techniques may outperform classical counterparts on electrophysiological detection tasks. This section describes the changing trends in optical electrophysiology research methods by focusing on electric field sensitive optical reporters such as genetically encoded voltage indicators (GEVIs), and quantum dots (QDs). We also discuss how

the status quo may be impeding translational success. This discussion focuses on two fundamental decisions that apply to all electro-optic reporters: the fractional intensity change of the reporter induced by the physiological signal of interest, $\Delta S/S_0$ (determined by the reporter's sensitivity), and the number of photons detected, n_s (set by the optical cross-section, and quantum yield of the reporter).

2.2.1. Electro-optic Considerations

A high signal-to-noise ratio (SNR) is a critical requirement for optical electrophysiology, and n_s detected during an electrophysiological experiment dictate it. Many primary and secondary issues rely on n_s . The primary includes electrophysiological measurements without an average, while the secondary includes available measurement time, which is frequently hampered by photobleaching and phototoxicity inherent in cutting-edge electro-optic measurements. The photons from an electrophysiological experiment do not just convey a pure “signal” to an imaging system. In an ideal camera (with a QE of 100 percent and no noise), a single pixel's SNR is subject to signal-dependent temporal uncertainty in the input, which manifests as temporal noise in the output. In other words, even the signal-to-noise ratio of a perfect camera is finite: it is a shot-noise-limited SNR (SSNR) value that real-world cameras can approach but never exceed. The SSNR can be estimated to be, $R_{S/N} \propto \Delta S/S_0 \sqrt{n_s}$. SSNR is a useful figure of merit when used to quantitatively evaluate an optical reporter under distinct photon flux conditions. Thus, the aforementioned equation serves as the foundation for the qualitative analysis presented in this review.

The following sections will critically review available optical electrophysiology options based on the SSNR equation for obtaining photon flux during an experiment.

2.2.2. GEVI

Genetically encoded voltage indicators (GEVIs) simultaneously monitor the membrane potential of multiple genetically targeted neurons via their expression in neural circuits^{35,56}. GEVIs are based on fluorescent protein fusions to a voltage-sensing domain and provide a strong optical response to membrane potential changes (Figure 2.2a). GEVIs robustly report both subthreshold events and action potentials in genetically targeted neurons (Figure 2.2b)³⁵. However, GEVIs have several disadvantages for in vivo bioelectric measurements: (1) measurements are shot noise limited due to a small number of available photons⁵⁷, and (2) they are difficult to use in humans due to its incorporation of the genetic indicator and the need to collect fluorescent signals from the brain⁵⁸.

The first issue is due to the small cross-sections of molecules (10^{-2} nm²)³² and quantum yields (QY $\sim 10^{-4}$ – 10^{-3})³³ leading to shot noise limited measurement. Shot noise reflects the quantal nature of light and the probabilistic nature of photon detection, is the dominant noise source in low-photon count measurements. We can consider two simple scenarios to demonstrate the effect of shot noise on signal detection. In the first scenario, the detector registers 10^6 photons per second, meaning that 1000 photons are recorded in each bin an average assuming 1 ms integration time. So, in the presence of an action potential (AP), a voltage reporter that experiences increased fluorescence signal by 10 percent will lead to 100 extra photons (signal) on

average in each bin. In the second scenario, the same detector registers 10^4 photons per second.

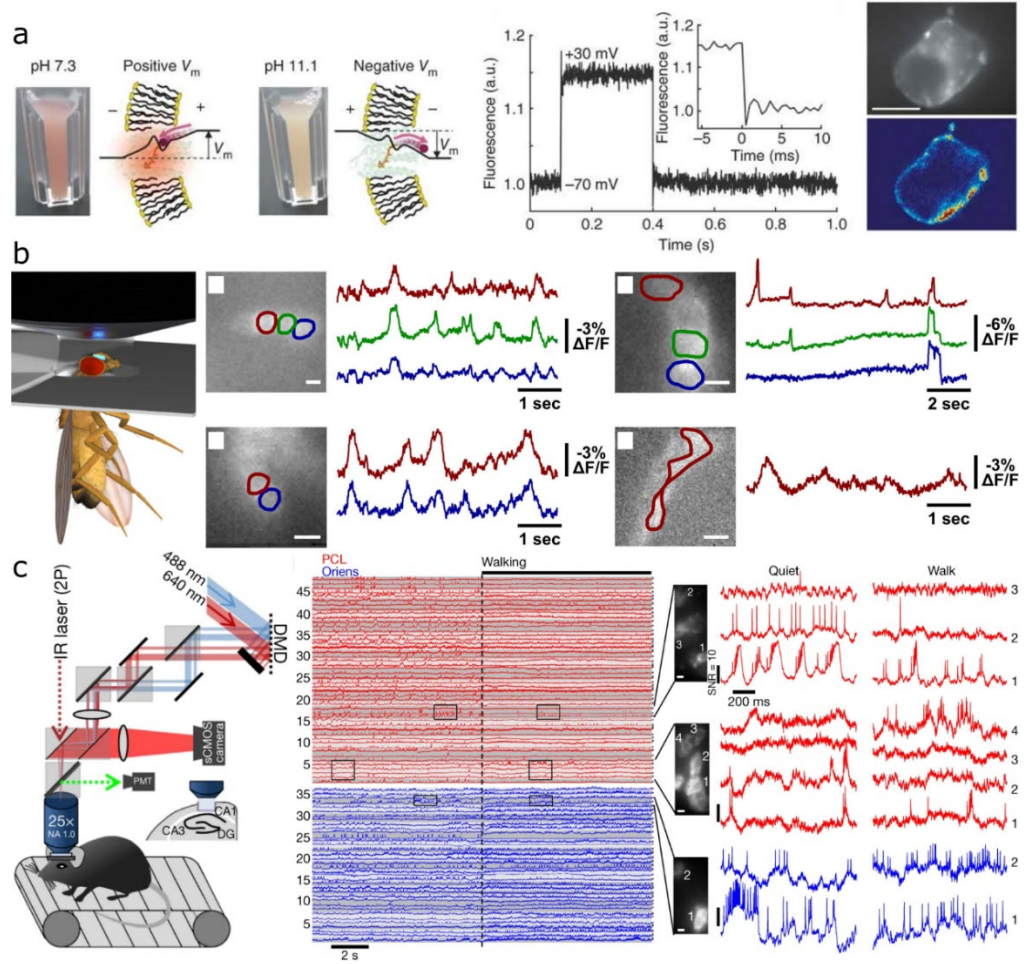


Figure 2.2. GEVIs. **a.** Mechanism of GEVI sensing where shifting membrane potentials alter the protonation and consequently the fluorescence (left). GEVIs under an applied voltage exhibits a step change in fluorescence (middle). An HEK 293 cell expressing the GEVI, Arch (right)⁵⁹. **b.** Setup diagram of in vivo recordings of a genetically modified fruit fly (left) and the results of recording spontaneous activity of clock neurons (right)³⁵. **c.** Setup for simultaneous two-photon (2P) imaging and patterned illumination (left) with fluorescence recordings before and during walking (middle). Portions of traces show complex spiking and subthreshold dynamics (right)⁵⁶.

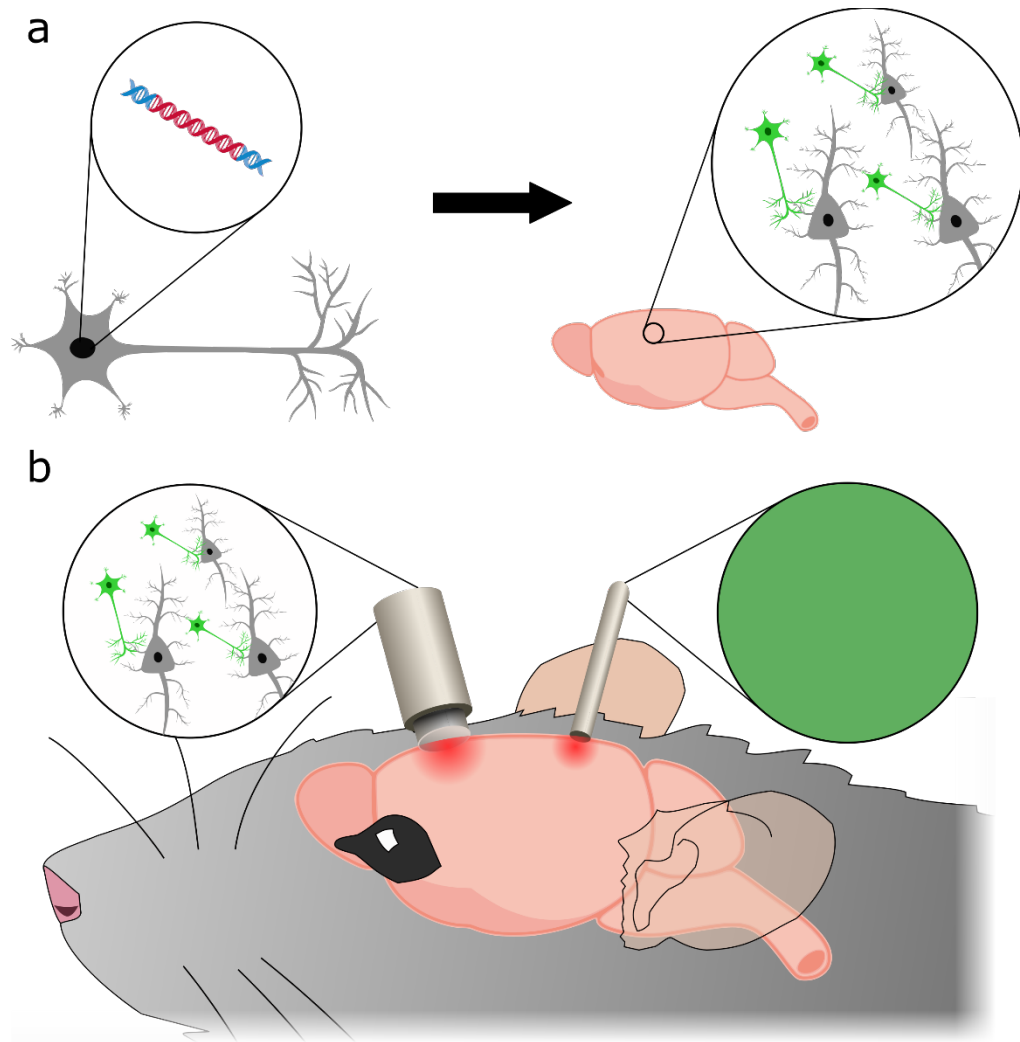


Figure 2.3. Issues of GEVI. **a.** Target neurons are genetically modified to express fluorescence, which is not feasible in human subjects. **b.** A GRIN lens or optical cannula can be used to observe in vivo fluorescent signals, but this requires invasive surgery.

Assuming identical excitation, detection conditions, and voltage reporters, each bin will contain one photon for the signal. Because shot noise is proportional to the square root of the number of available photons detected during an experiment $R_{S/N} \propto \Delta S/S_o \sqrt{n_s}$, the second scenario will be shot noise limited $[(\Delta S/S_o)n_s \leq \sqrt{n_s}]$. As a result, even for GEVIs that have excellent voltage sensitivity (40%)⁶⁰, real-time

measurement of electrophysiological signals is not possible with them for low light levels (<25 per bin). Of course, this is solved by using higher intensities with GEVIs, but this leads to photobleaching and phototoxicity which complicate measurements and harm the sample.

The second issue with GEVIs is that they require genetic mutations to be incorporated into the cell membrane (Figure 2.3a). As a result, the use of GEVIs necessitates gene delivery via a vector, which is usually a virus. This entails injecting a virus containing genetic material to reprogram that of host cells into expressing GEVIs on their membranes. Testing different virus dilutions to achieve optimal expression is critical because either too little expression leads to no signal or too much expression leads to high fluorescence background noise and cell death⁶¹. Additionally, the GEVI viral vector must be able to express in the target cells at target locations, which is determined by the tropism of the virus- its ability to infect a certain biological arena. For some neurons there is no present compatible tropism to allow for the use of GEVIs, and for many it is challenging to target the whole cell instead of just the soma for instance⁶². In vivo GEVI experiments also necessitate the surgical implantation of an imaging probe, such as an optical cannula, GRIN lens, or similar device, to collect fluorescent signals from the brain (Figure 2.3b). GEVIs are currently being tested in animal models such as mice due to the advancement of genetic mouse models; however, the use of GEVIs in humans is unlikely in the near future^{58,63}.

2.2.3. Quantum Dots

Quantum dots (QDs) offer larger cross sections compared to GEVIs (1 nm^2 QDs vs. $\sim 10^{-2} \text{ nm}^2$ GEVI)^{32,64}. As a result, a relatively large number of photons, n_s , are detected during an electrophysiological experiment, which consequently improves SSNR according to $R_{S/N} \propto \Delta S/S_0 \sqrt{n_s}$.

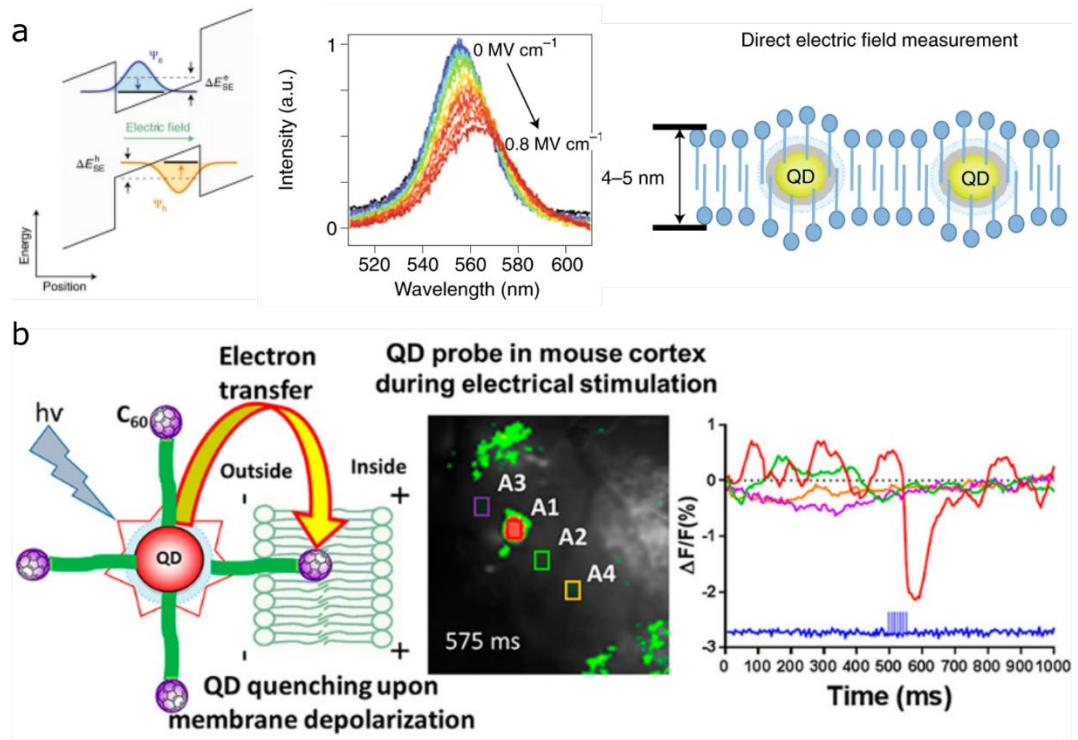


Figure 2.4. Quantum Dots. **a.** In the quantum confined Stark effect, electric fields applied to QDs shift the wavefunctions of charge carriers and consequently affect the photoluminescence of the QD (left). Applied electric fields quench and redshift QD photoluminescence (middle) and it's ideal for QDs to nestle within the plasma membrane to experience the highest electric field (right)³⁶. **b.** QD-peptide-fullerene bioconjugates anchor themselves to the plasma membrane (left) and were used in mouse cortex to detect bursting behavior (right)⁶⁵.

The electric field sensitivity of QDs arises via the quantum-confined stark effect (QCSE) (Figure 2.4a). The QCSE occurs in quantum-confined systems such as QDs when subjected to an electric field applied along the confinement axis⁶⁶. Utilizing this

effect, QDs have been shown to detect action potentials in vitro and in vivo. QDs covered in a biocompatible coat can adhere to plasma membrane surfaces to then sense nearby fields for optical recording (Figure 2.4b). QD's high cross-section compared to molecular reporters makes them useful for neuroscience methodologies. QDs can provide ~11% change in photoluminescence signals for an applied field of 10 mV/nm. However, in the context of electrophysiological detection this electro-optic effect is not that high as compared to other fluorescent reporters that show 25-40%⁶⁰. $\Delta S/S_0$ drops further during an extracellular measurement and as a result, QDs fall short of being an efficient field reporter with a large optical cross-section and high sensitivity to electric fields, which is ultimately what is needed for successful large-scale measurements.

2.2.4. Plasmonic

Plasmonic nanoresonators with exceptionally large cross sections ($\sim 10^4$ nm²) offer orders of magnitude enhanced photon-flux (n_s) measurements compared to GEVIs or QDs. Plasmonic nanoresonators do not show photostability and phototoxicity limitations or require invasive genetic incorporations like GEVI. Strongly enhanced near fields associated with plasmonic modes facilitate the transduction of tiny fluctuations in the local refractive index to readily detectable resonance wavelength shifts in the far-field spectra without any physical connections⁶⁷. However, the main weakness of the plasmonic field reporters is their low inherent electric-field sensitivity. Electro-optic effects, alterations in metal plasma frequency, $\Delta\omega_p (= \Delta n_e \omega_p / (2n_e))$, in plasmonic metals (e.g., Au, Ag, etc.) associated with non-Faradaic (electric double layer) charging/discharging are very weak because of extremely high electron densities,

n_e (e.g., for Au, n_e is $\sim 10^{23} \text{ cm}^{-3}$). As a result, optical field measurements using plasmonic nanostructures are readily dominated by shot noise due to small $\Delta S/S_o$ (according to $R_{S/N} \propto \Delta S/S_o \sqrt{n_s}$).

2.2.5. Electro-plasmonic Nanoantennas

To overcome the problems with existing electro-optic translators, my colleagues at the Habib et al. recently pioneered a new class of extremely bright label-free optical (wireless) field probes termed electro-plasmonic nanoantennas with dramatically improved field sensitivity and signal-to-shot-noise ratio. These improved characteristics are largely the consequence of active lumped nanocircuit elements that are analogous to tunable radio frequency (RF) antennas (Figure 2.5a), which introduce an electric field-controlled load enabling active and reversible tuning of the plasmonic resonances (Figure 2.5b). As a load, they used biocompatible electrochromic polymer poly(3,4-ethylenedioxythiophene): polystyrene sulfonate (PEDOT: PSS) to coat gold plasmonic nanoantennas (Figure 2.5c). Electrochromic materials known to have optical properties that can be reversibly modulated by an external field are conventionally used for smart glass/mirror applications. However, this operation is slow (~ 1 s) and requires a large, applied field⁶⁸. At nanoscale dimensions, electrochromic materials can respond faster. Furthermore, thicker films are desirable to achieve strong electro-optic signals. In the case of electro-plasmonic nanoantenna case, optical readout of the electrochromic material state is enabled by the enhanced light matter interaction through plasmonic particles.

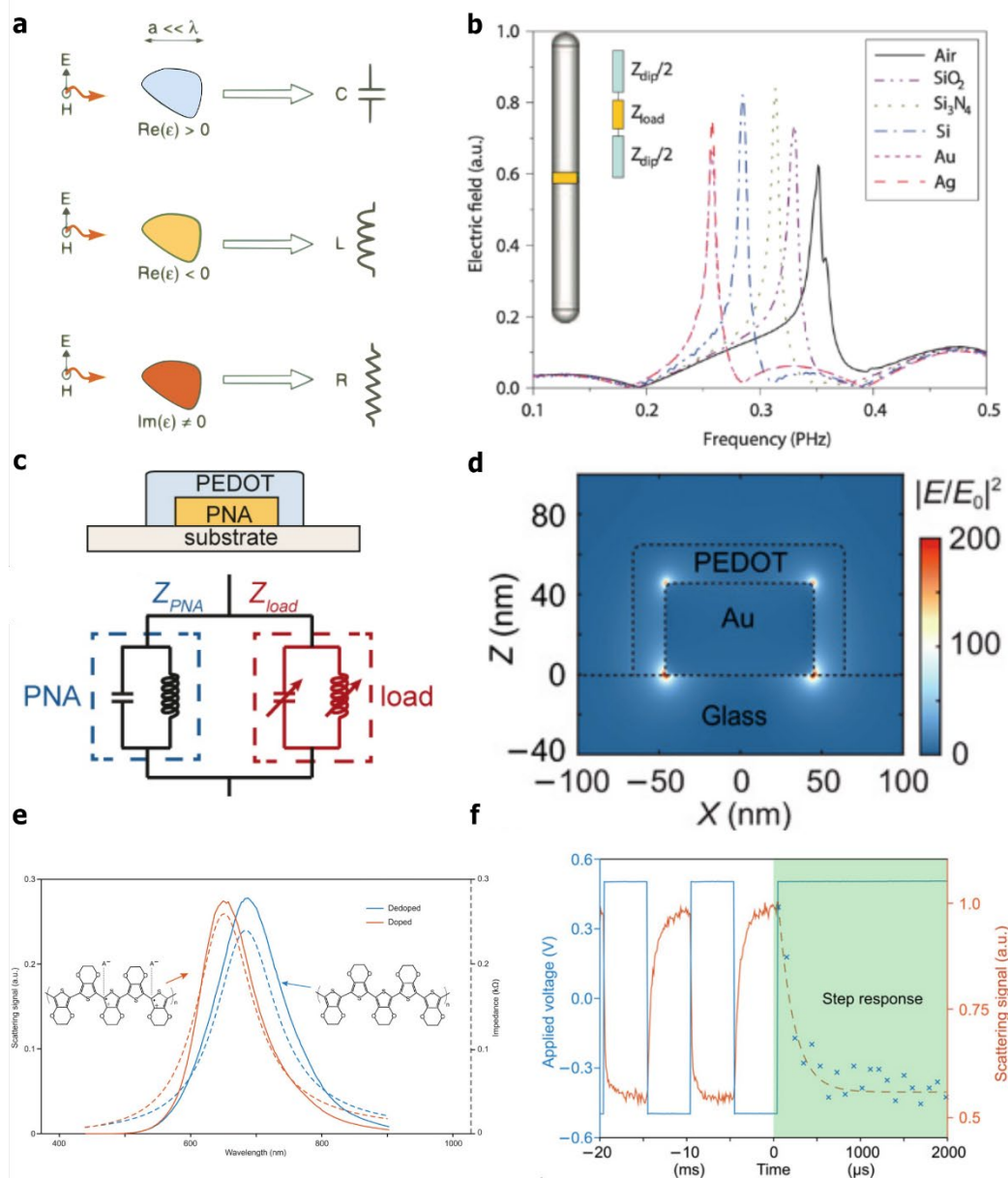


Figure 2.5. Nanoantenna loading. **a.** Different optical materials are akin to different circuit elements in an optical circuit⁶⁹. **b.** A gap nanoantenna exhibits large shifts in its scattering spectrum for different gap materials⁷⁰. **c.** A plasmonic nano-resonator acts like an LC resonator and is effectively modulated with an electrochromic polymer load. **d.** Electro-plasmonic nanoantennas confine light below the diffraction limit to produce high intensity hot spots. **e.** The spectrum of electro-plasmonic nanoantennas blue-shifts under an applied field (red, doped) and redshifts when the field is reversed (blue, de-doped). **f.** Electro-plasmonic nanoantennas experience sub-millisecond electrochromic switching times under an applied square wave potential¹⁴.

By taking advantage of drastically enhanced light-matter interactions in these plasmonic hotspots (Figure 2.5d), it is possible to simultaneously achieve strong electro-optic sensitivity. Electric fields applied to electro-plasmonic nanoantennas alters charge carriers in the electrochromic polymer and modulate its optical properties. This shift in optical properties is detected remotely through the coupled plasmonic nanoantenna resonances, which experience a large shift in its scattering spectrum (Figure 2.5e). Additionally, it is possible to achieve a fast electrochemical response using ultrathin electrochromic loads. This is demonstrated in controlled experiments with a square wave potential applied to yield the optical response; by fitting an exponential to the step response, sub-millisecond ($\sim 200 \mu\text{s}$) electro-optic response times are shown (Figure 2.5f).

The drastically enhanced cross-section (i.e., high n_s) and ultrahigh field sensitivity (i.e., high $\Delta S/S_0$) of the electro-plasmonic nanoantennas result in high SSNR according to $R_{S/N} \propto \Delta S/S_0 \sqrt{n_s}$ (Figure 2.6a). Even weak extracellular fields generated by spiking electrogenic cells can lead to optically measurable changes in the electrochromically loaded plasmonic antennas or electro-plasmonic nanoantennas (Figure 2.6b). Use of electrochromic materials is also adapted by other groups using total internal reflection based light confinement into a thin PEDOT:PSS layer (Figure 2.6c). However, this requires a complex optical arrangement. Although it is possible to use waveguides for BMI, the advantages offered are lost due to similar limitations of MEAs related to physical implantation and wiring.

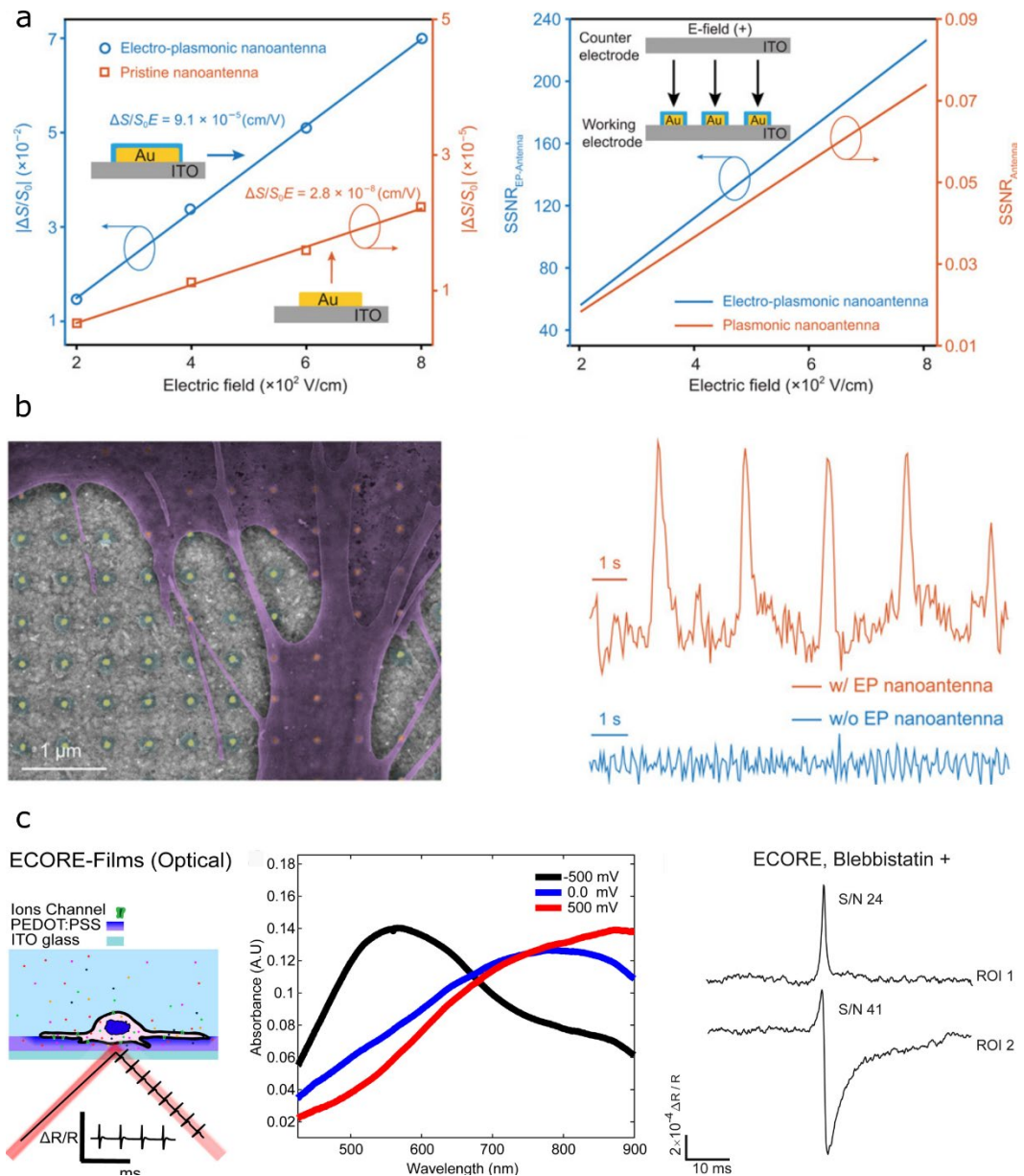


Figure 2.6. Electro-plasmonic biosensing. **a.** Electro-plasmonic nanoantennas show vastly greater sensitivity to electric fields over bare plasmonic nanoantennas (left). Both electro-plasmonic and bare nanoantennas were placed in a parallel plate configuration with an ITO electrode to test their sensitivity to electric field where electro-plasmonic nanoantennas show very high SSNR, especially compared to bare plasmonic nanoantennas. **b.** Cardiomyocytes were cultured on a substrate of electro-plasmonic nanoantennas (left) and their scattering signal was recorded to reveal spiking at regular intervals (right)¹⁴. **c.** SPR biosensing setup for neuronal sensing (left). The plasmonic surface will change its absorbance while under different potentials (middle), which can be used to sense action potentials (right)⁷¹.

Unlike this waveguide-based approach, electro-plasmonic nanoantennas can wirelessly convert the cell's local electric field dynamics in the kHz range to modulations in the high frequency electromagnetics of the plasmonic resonator.

2.3. Methods for Bulk Activity

The optical and electrical methods discussed thus far operate by transducing electric fields or potentials, however, this is exceptionally challenging to apply to whole brain measurement in humans. To do so using electrical methods would require disbursing electrodes throughout the entire brain, which would not only require extraordinary labor, but would also be extremely invasive and likely damaging⁷². The optical methods described cannot be used in humans for many reasons including requiring genetic modification, phototoxicity, and a severe lack of sensitivity¹². Additionally, many use wavelengths which experience high scattering in brain tissue, so even with the advantage of a craniotomy (opening of the skull) the available depth of interrogation would be on the order of millimeters at best⁷³. To circumvent these limitations, other techniques target indirect, hemodynamic indicators of activity.

2.3.1. fNIRS

Near-infrared (NIR) spectrometry methods have recently received a lot of attention for BMI applications due to numerous advantages such as safety, portability, wearability, ease of use, and more⁷⁴. In the wavelength range 740-2500 nm, NIR light shines through the skull to the brain and is known to have the best penetration (~3 to 5 cm) into biological tissue (Figure 2.7a)⁷³. Functional Near Infrared Spectroscopy (fNIRS), which detects brain activity using 740-900 nm light, is a novel NIR based signal

acquisition tool for BMIs (Figure 2.7b). Unlike GEVIs, fNIRS monitors brain activity without the need for genetic modification or labeling. fNIRS does not measure the electrical activity of the brain directly, but rather the metabolic activity of regions through variations in hemoglobin concentrations. fNIRS takes advantage of differences in the optical properties of oxyhemoglobin (HbO) and deoxyhemoglobin (HbR), which fluctuate due to neural activity. Patterns of oxygenation amongst regions of the brain can provide distinguishing features of mental illness, cognitive and motor function (Figure 2.7c), and more^{75,76}.

There are two primary analyses in commercial fNIRS systems: continuous wave (CW) and time-domain (TD) fNIRS⁷⁷. CW fNIRS constantly illuminates target tissue to monitor relative changes in blood flow and oxygen. This is the original and most prevalent method in fNIRS. TD fNIRS delivers pulses of NIR light less than a nanosecond in duration and records the returned light which is comprised of a light distribution that is stretched in time compared to the initial pulse due to random scattering events among photons. Scattering properties of tissue can be determined by analyzing the area under the curve of the distribution, its maximum photon time-of-flight (time spent from source to detector), and the width of the distribution⁷⁸. fNIRS estimates tissue optical properties such as absorption (μ_a) and reduced scattering (μ_s) coefficients by parameterizing the distribution of photon arrival times (Figure 2.7d). Systems which utilize TD fNIRS convey more information, but at the expense of having much more complex hardware and analysis. A number of fNIRS systems are available now based on the newer TD fNIRS, and because of their higher information

content than CW systems, time-domain TD-fNIRS systems are considered the gold standard for optical brain imaging systems⁷⁹.

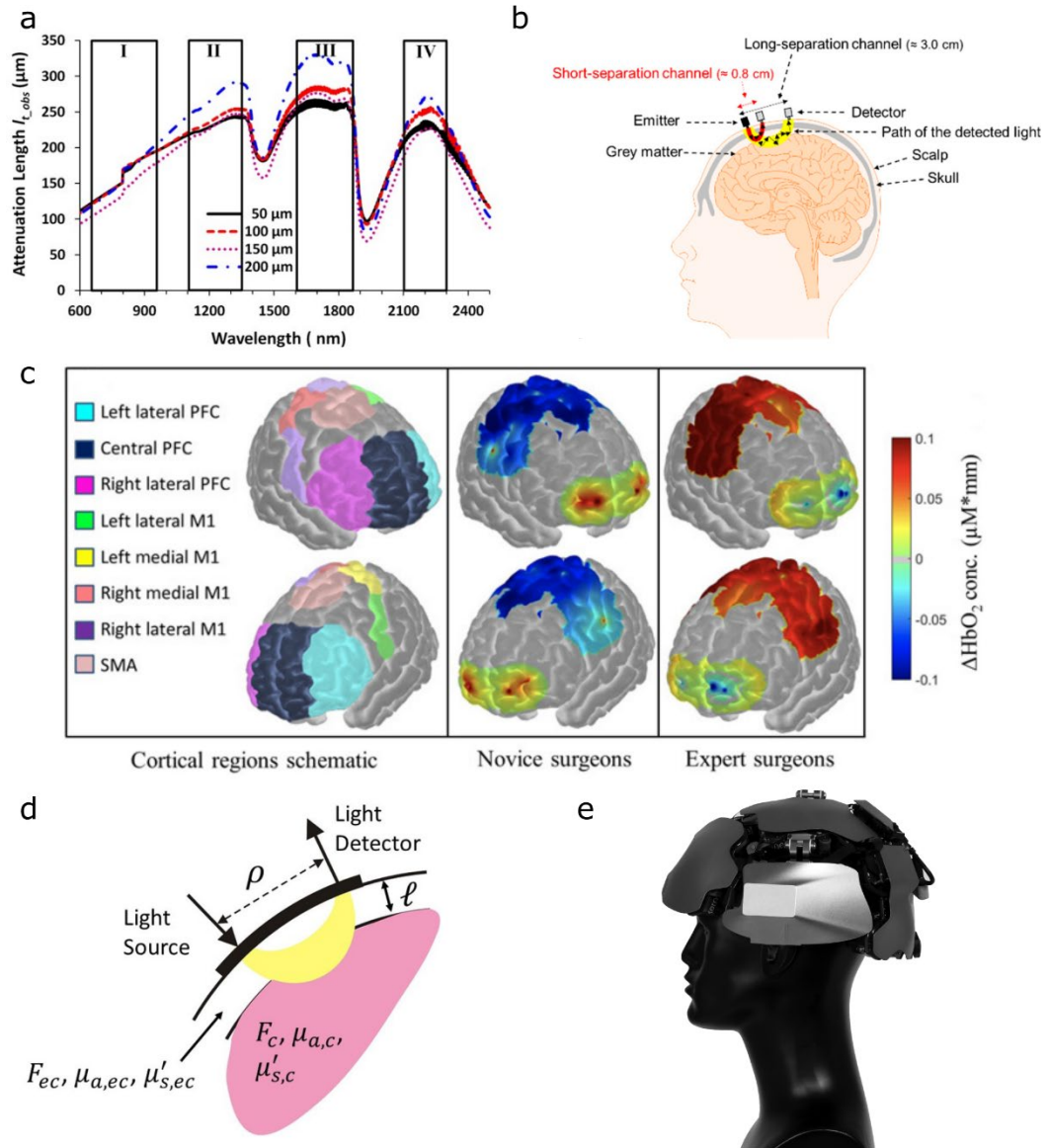


Figure 2.7. NIR Imaging. **a.** Attenuation length of NIR light through biological tissue shows four windows which are good for biological imaging⁷³. **b.** Diagram of simple functional NIR spectroscopy (fNIRS) where a short and long separation channel measure light intensity received from an emitter⁸⁰. **c.** fNIRS recording of different brain regions differentiates between novice and expert surgeons⁷⁵. **d.** NIR light travels in a curved path through the brain, which is longer than the source-detector distance⁸¹. **e.** The Kernel Flow system covering whole-head measurement⁸².

Since the 1980's, fNIRS have been used in psychiatry to investigate new biosignatures of mental illness and conditions⁸³. Using fNIRS, regional activity across the whole brain can be investigated while the subject participates in a natural setting⁸⁴. Very recently, Ban et al. have developed “Kernel Flow,” a wearable, whole head coverage TD-fNIRS system that allows for inexpensive commercial production due to scalable manufacturing in contrast to other TD-fNIRS systems (Figure 2.7e)⁸². The compact design of the Kernel Flow system enables the use of TD-fNIRS in a wider range of applications.

Despite adequate transfer of NIR light through the skull, the small absorption cross-section of hemoglobin limits the signal strength of fNIRS. The diameter of a single hemoglobin molecule is about 5 nm, and the absorption cross-section is even smaller than its physical cross section⁸⁵. The signal obtained from fNIRS depends on light interaction with hemoglobin and its SSNR suffers as a result of its poor scattering capabilities. Moreover, the physics of freely scattered light through the brain without the use of a contrast agent limits the spatial resolution of fNIRS⁸⁶. High scattering cross-section electro-plasmonics are poised to make use of the biological transparency of NIR without the SSNR and resolution limitations faced by fNIRS.

2.3.2. fMRI


Like fNIRS, functional magnetic resonance imaging (fMRI) is a popular neural imaging modality because it is non-invasive, and it has the added benefit of being prevalent in clinics for standard magnetic resonance imaging (MRI)⁸⁷. However,

instead of using light, fMRI uses magnetic fields and radio frequencies (RF) to image hemodynamic and metabolic activity in the brain⁸⁸.

MRI

Atoms with an odd number of protons, neutrons, or both have nuclear spin, and in a strong magnetic field, nuclear spins will undergo precession around the axis of the applied magnetic field (Figure 2.8a) at a frequency $\omega_0 = \gamma B_0$ where γ is the gyromagnetic ratio and B_0 is the magnetic field strength. Some spins are parallel, others antiparallel, and nearby opposing spins will negate each other aside from a small excess of spins in the direction of magnetic field which create a net magnetization macroscopically⁸⁹.

RF at the precession frequency, ω_0 , can influence this precession; by applying a RF pulse with transverse fields perpendicular to the applied magnetic field, spins will gain a precession component perpendicular to the magnetic field. The result is a generation of oscillating magnetic flux as spins precess in and out of alignment with the applied field. The raw MRI signal is the voltage on a large, sensitive coil that changes as a result of this magnetic flux. Because transverse precession is induced by a finite RF pulse, this oscillating signal will decay over time as spin precessions become out of phase with each other and is known as free induction decay (FID; Figure 2.8b, left). The time constant of the FID envelope is T_2^* , which is generally much shorter than a decay time constant caused by randomly varying fields in the system, T_2 . Miniscule inhomogeneities in the magnetic field cause spins to de-phase much faster than

expected, which poses a problem for MRI. MRI differentiates between tissues by measuring the FID from volume to volume, but if only the much smaller T_2^* is given, then the differences between tissues are also much smaller and tissue contrast is substantially reduced if not lost entirely⁸⁸ 

However, by applying a 180° RF pulse some time, t_e , after applying the previously mentioned perpendicular 90° pulse, spins will begin to “rephase” and exhibit another smaller peak signal at $2t_e$ called a spin echo which then decays due to dephasing in the opposite direction. The peak of the spin echo is less than that of the original pulse due to random field fluctuations and is enveloped in a larger exponential decay with time constant T_2 (Figure 2.8b, right). Measuring these spin echoes allows us to fit another exponential to their peak values and extract T_2 to get a much better SNR in differentiating tissues.

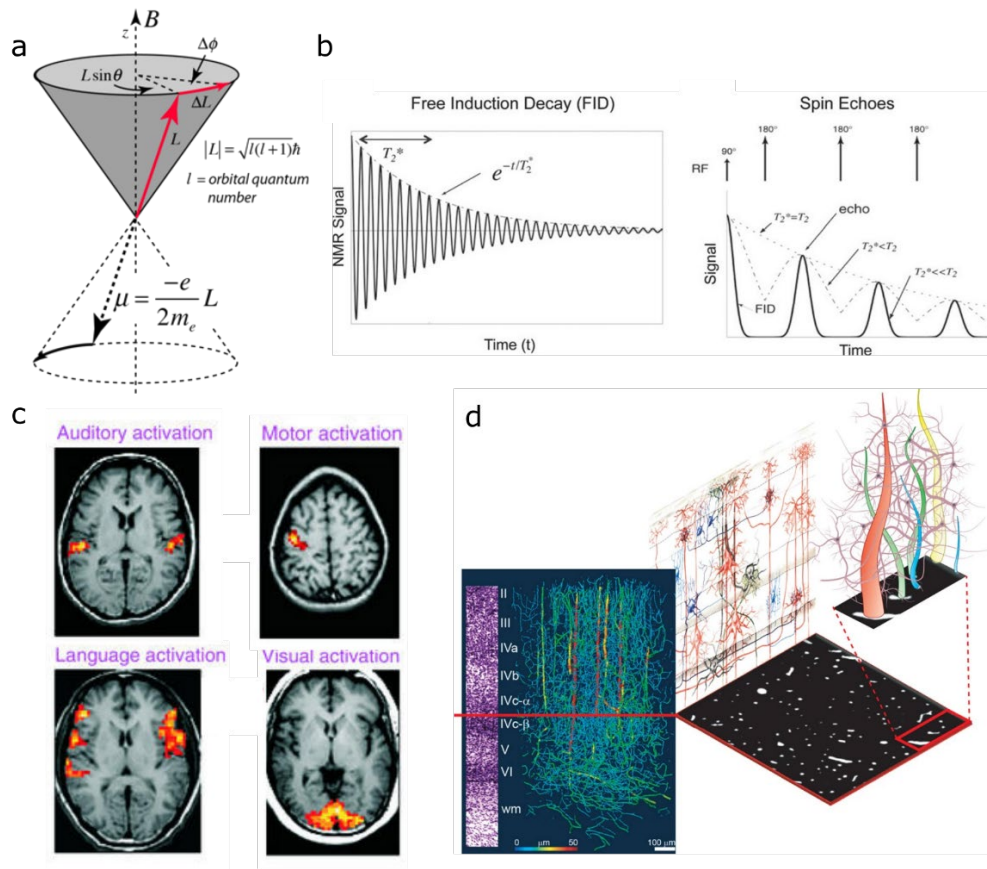


Figure 2.8. Functional magnetic resonance imaging (fMRI). **a.** Nuclear spin precession around the axis of magnetic field, B ⁸⁹. **b.** Fundamental oscillatory magnetic resonance signal known as free induction decay with decay time constant T_2^* (left) and spin echoes (right) showing times of RF pulses and the T_2 envelope⁸⁸. **c.** fMRI data showing activation of different functional regions in the brain⁹⁰. **d.** Blood vessels inside the visual cortex of a monkey recorded by X-ray microtomography demonstrating that most of the brain is not composed of vasculature. The circulatory structure appears dense when looking at the 3D structure on the left, but a slice reveals that only 3% is composed of blood vessels; there is a vast host of cell diversity and activity between blood vessels which is immeasurable using fMRI⁹¹.

fMRI

The development of fMRI became possible when enhanced, one-shot imaging methods were introduced to capture MRI image data in 20-30 milliseconds^{87,92}. The most common one-shot method is known as echo planar imaging (EPI), where 2D

pulsed linear magnetic field gradients are applied to the subject and the inverse Fourier transform of the time-dependent magnetic resonance signal will allow for the reconstruction of a functional image⁹³. fMRI is useful for determining which regions of the brain are active, and trained experts can deduce the functionality associated with areas of activation (Figure 2.8c)⁹⁰. However, this fMRI technique is limited in spatial resolution to $3 \times 3 \times 3 \text{ mm}^3$ by the wavelength of field gradients used in recording⁹⁴, and experiences a number of drawbacks.

The limitations associated with fMRI primarily concern its resolution in time and its transduction of bulk effects as opposed to the electrophysiology of the brain. The time it takes to acquire fMRI data is ultimately limited by the dynamics of nuclear spin dephasing, which occur on the order of tens of milliseconds, so whole brain imaging occurs on the order of seconds despite using sophisticated methods to capture multiple slices simultaneously— still three orders of magnitude slower than neuron action potentials⁹⁵. Moreover, there is no way to extract electrical activity of cells with fMRI.

The current standard in processing fMRI data is based on the BOLD response, which is primarily driven by the change in local deoxyhemoglobin concentration⁹⁶. Deoxyhemoglobin is paramagnetic, which gives deoxygenated blood an increased magnetic susceptibility and results in a decreased magnetic resonance signal. An increase in neural activity induces a large change in cerebral blood flow (CBF), which supplies more oxygen to active regions than they will deplete metabolically ultimately resulting in a boosted magnetic resonance signal. BOLD depends on the combined

changes of CBF, cerebral metabolic rate of oxygen (CMRO₂), and the cerebral blood volume (CBV)⁹⁴. One issue is that increased neural activity tends to increase each of these physiological variables, but these changes have conflicting effects on the BOLD response. As CBV increases, deoxyhemoglobin is washed away and increases the BOLD signal, but increasing CMRO₂ adds to surrounding deoxyhemoglobin concentration and lowers BOLD⁸⁸. Innovations in BOLD fMRI are attempting to use new imaging methods to parse the variables bundled in the BOLD response with better spatiotemporal resolution^{97,98}. Measuring the BOLD response is useful for showing the metabolic and circulatory activity of brain regions, but it is fundamentally limited in its functional analysis of the brain by those measures.

Recent developments in fMRI are focusing on boosting spatiotemporal resolution by increasing the magnetic field used or improving the coil design⁹⁹. Other innovations seek to measure different parameters using magnetic resonance like arterial spin labelling to measure CBF or diffusion tensor imaging (DTI) to image the diffusion coefficient of water which is used in the Human Connectome Project among other techniques to make a large scale map of functional connectivity in the brain^{95,100}. This is exciting work that will expound on our understanding of the brain functional map, but fMRI must be paired with other methods to obtain electrophysiological activity.

3. Electro-plasmonics for High-throughput Neural Sensing

Since Hermann von Helmholtz's first measurement of nerve impulses in 1849, electrophysiologists have been developing tools to gain simultaneous access to the

activity of every cell in a network in order to advance collective understanding in cardiology and neuroscience¹⁰¹. Yet, progress towards this goal remains elusive due to the difficulty of recording many cells over large area with high spatial resolution. Leading imaging technologies such as GEVIs¹⁰² and MEAs^{42,103} still have several drawbacks, including long-term measurement instability and limited scaling capacity. State-of-the-art MEAs, commonly known as HD-MEAs, although focusing on getting larger arrays with more electrodes, still have limited spatial resolution (pitch $>10\ \mu\text{m}$; electrode diameters $>10\ \mu\text{m}$), and number of electrodes ($<70\ \text{k}$)^{104,105}. This is due to the trade-off between signal-to-noise-ratio (SNR) and number of readout channels. A MEA read-out channel requires on-chip signal conditioning elements including amplification and filtering circuitry that sets the minimum footprint of a recording site ($>10\ \text{mm}^2$). Also, the number of recording channels is limited by the tighter upper limits for low-noise transmission of spiking cell signal by multiplexed data channel. Therefore, state-of-the-art high density MEAs to date only can achieve limited electrode density 1000-5000 electrode per mm^2 . On the other hand, optical imaging tools exploit the unprecedented (time/wavelength division) multiplexing and information carrying capabilities of light and have the potential to be an ideal candidate for the high-throughput electrophysiological imaging with high spatial-temporal resolution to capture electrical activity at subcellular, single-cell and network levels. However, state-of-the-art optical tools typically require high-intensity light to maintain a good SNR due to the limited number of photons available during measurement. As a result, it is difficult to measure the electrophysiological signal without an average that makes the

imaging speed slow. Recently, there has been a push to develop electro-optic translators by harnessing the effective refractive index modulation of electrochromic material due to an applied electric field^{14,71}. These types of probes generally tend to have more detected photons, minimizing the likelihood of low-SNR measurements without averaging. However, electrochromic based electro-optical translators developed so far are limited to measurements of cell activity at the network level and therefore cellular activity at single cell resolution remains unexplored.

Here I present high-density ~ 3 million electrodes per mm^2 , and wireless nanoelectrode array (W-NEA) that enables electrophysiological imaging of network of cell with a subcellular resolution. We arrange a larger number of nanoelectrodes (~ 500 million) with high spatial resolution (~ 560 nm). Importantly, each electrode is sensitive to the local electric field around it and each electrode could be used to detect the activity of the cell. To ensure excellent signal-to-shot-noise ratio with a single nanoelectrode, W-NEA uses a plasmonic nanohole geometry that takes advantage of the extraordinary optical transmission (EOT) effect¹⁰⁶. The EOT effect allows for a much greater amount of light to pass to the detector using collimated optics without the need for dark-field microscopy that was used in a recent previous study based on electro-plasmonic nanoantenna array¹⁴. We demonstrate a higher sensitivity of one order of magnitude with W-NEA compared to the electro-plasmonic nanoantenna array. Our objective is to demonstrate image the electrical activity of a network of cell containing many cells with single cell resolution. To image the action potential propagation, neonatal cardiomyocytes (CMs) are cultured over the surface of W-NEA.

The W-NEA contains >22- millions of electrodes within a $2662.4 \times 2662.4 \mu\text{m}^2$ (FOV of the imaging system). We show that W-NEA can detect thousands of electrogenic cell in a large $2662.4 \times 2662.4 \mu\text{m}^2$ area with a single cell resolution.

3.1. Wireless Nanoelectrode Arrays (W-NEAs)

The W-NEA imaging system has optical access to electrophysiological cells within the FOV area over which electrophysiological activity can be detected with better than single cell resolution as: I) each nanoelectrode acts independently and serves as a local electric field variation reporter (Figure 3.1a), and II) nanoelectrodes in the W-NEA are spaced 560 nm apart, offering resolution two orders of magnitude smaller than a single cardiomyocyte as shown by the sheer scale difference in Figure 1a-inset. Nanoelectrodes of W-NEA are composed of a biocompatible electrochromic polymer poly(3,4-ethylenedioxythiophene)- hexafluorophosphate (PEDOT-PF₆)¹⁰⁷ ‘electrochromic load’ coupled to metallic nanoholes.

3.1.1. W-NEA Fabrication

To fabricate the device (W-NEAs with a periodicity 560 nm and hole diameter 280 nm loaded with 25 nm thick PEDOT layer) we employ deep-UV photolithography and electrochemical deposition techniques (Figure 3.1). Gold is evaporated onto glass as well as titanium as an adhesion layer. Photoresist is spun onto the wafer and exposed in the pattern of the nanoholes. Development exposes holes in the photoresist, which are targeted with ion beam etching to produce holes in the gold/titanium layer. Subsequently, the remaining resist is stripped, and the device cleaned prior to

electrodeposition of PEDOT:PF₆. Following electrodeposition, the device is thoroughly dried with a nitrogen gun and ready for use.

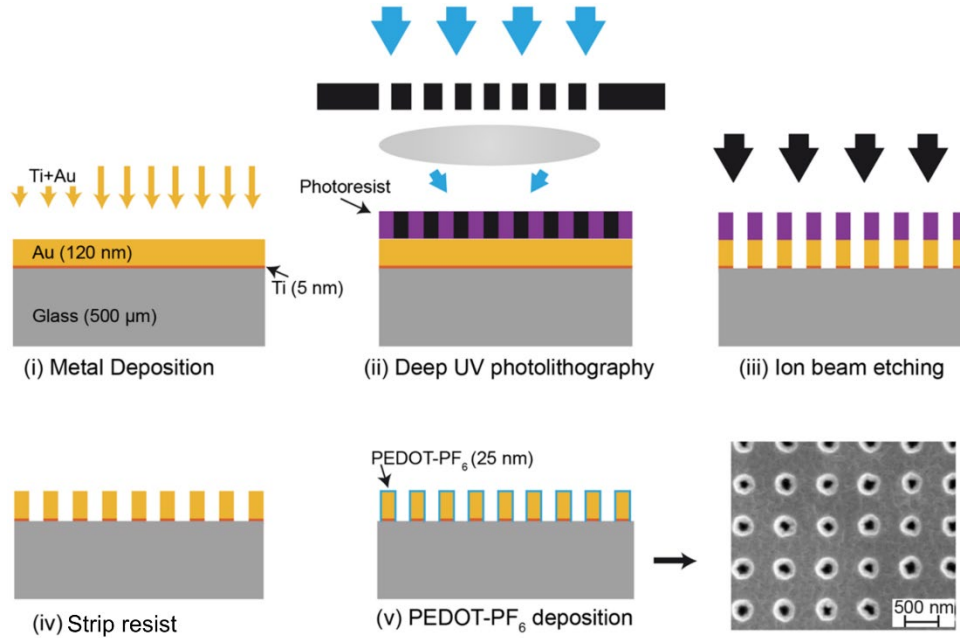


Figure 3.1. Sequential steps to fabricate W-NEA using photolithography and electrodeposition. The final result is a periodic array of nanoelectrodes as seen by SEM.

3.1.2. Optical Circuit Model

The working principle of the W-NEA is based on the active tuning of electrochromic loading (doping levels) via the extracellular electric field and the alteration of plasmonic resonances. At resonance, the subwavelength holes squeeze optical field beyond the diffraction limit and enhance optical field (‘plasmonic hot spots’) that are orders of magnitude greater than the incident optical field. Figure 3.1b indicates that hot spots occur at the edge of the nanohole in a square periodic array. The unprecedented way of light management at plasmonic resonances lead to highly intensified interactions between light and electrochromic loading. Hence, a significant

change in light transmission through the nanoholes occurs when an applied electric field (e.g., extracellular electric field) modulates the effective refractive index, ϵ_{eff} , of the PEDOT-PF₆ electrochromic load (Figure 3.1c). The unconventional light transmission through sub-wavelength W-NEAs, known as extraordinary light transmission (EOT), requires coupling of the plasmonic modes: (i) surface plasmon polariton (SPP) propagating on the surface of the nanoholes created through the periodicity; and (ii) localized surface plasmon (LSP) at the rims of the nanoholes. The complex interplay between plasmonic modes could be easily understood using our phenomenological coupled RLC circuit model (Figure 3.1c inset). Following our FDTD analysis in Figure 3.1b, equivalent circuit model consists of three RLC oscillators corresponding to SPP modes on the gold-PEDOT side (in-coupling SPP mode, SPP_{in}) and on the gold-glass side (out-coupling SPP mode, SPP_{out}), and LSP modes at the rims of the nanoholes. The coupling between the SPP_{in} and SPP_{out} oscillators is realized through LSP oscillator. Lumped circuit elements, the inductors L_1 , L_2 , and L_3 , and the capacitors C_1 , C_2 , and C_3 control the oscillation of the corresponding plasmonic excitations. Within the first approximation, the PEDOT load controls the LSP resonances by the intense interaction between the light and the PEDOT load within the hot spots. The electrochromic doped/de-doped level is therefore incorporated into the LSP loop as a parallel arm, consisting of tunable inductive and capacitive circuit elements. Resistors are added to each oscillator for radiative and non-radiative losses. The equivalent impedance Z_{eq} of the electro-plasmonic circuit regulates the power $P(=|V_s|^2/Z_{\text{eq}})$ supplied by the voltage source, the

circuit equivalent of the transmitted light intensity through the W-NEA. Here, Z_{eq} is a combination of equivalent resistance R_{eq} and equivalent reactance X_{eq} ($Z_{eq}=R_{eq}+jX_{eq}$; j complex number). Figure 3.1c shows the EOT resonance for the doped (blue curve) and the de-doped (red curve) electrochromic doping level. The EOT resonance consists of multiple peaks (maximum power delivery) and dips (minimum power delivery) based on SPP-LSP coupling. Minimum power delivery (minimum light transmission) occurs when the equivalent reactance X_{eq} is projected to a circuit consisting of parallel inductive and capacitive reactances, operating at the resonance condition $\omega^2=L_{eq}C_{eq}$. Hence, a large impedance is seen by the voltage source V_s due to the cancellation of equivalent inductive and capacitive reactances $X_{eq}=\omega^2L_{eq}C_{eq}/(j\omega L_{eq}-j/\omega C_{eq})$. The large impedance results in minimum power delivery at the resonance dips. The maximum power delivery (maximum light transmission) occurs as a result of the cancellation of equivalent inductive and capacitive reactances ($X_{eq}=j\omega L_{eq}-j/\omega C_{eq}$) that are in series at the operating frequencies. Increased load inductance and capacitance due to load de-doping results in a red-shifted spectrum (Figure 3.1d, red curve) compared to a doped state (Figure 3.1d, blue curve). The drastic change in the intensity of the light could be used to detect extracellular electrical fields using a camera with high sensitivity. The findings of our circuit model are in close agreement with our experimental measurements and successfully capture the complex EOT spectrum profile coupled to the doping level of the PEDOT load.

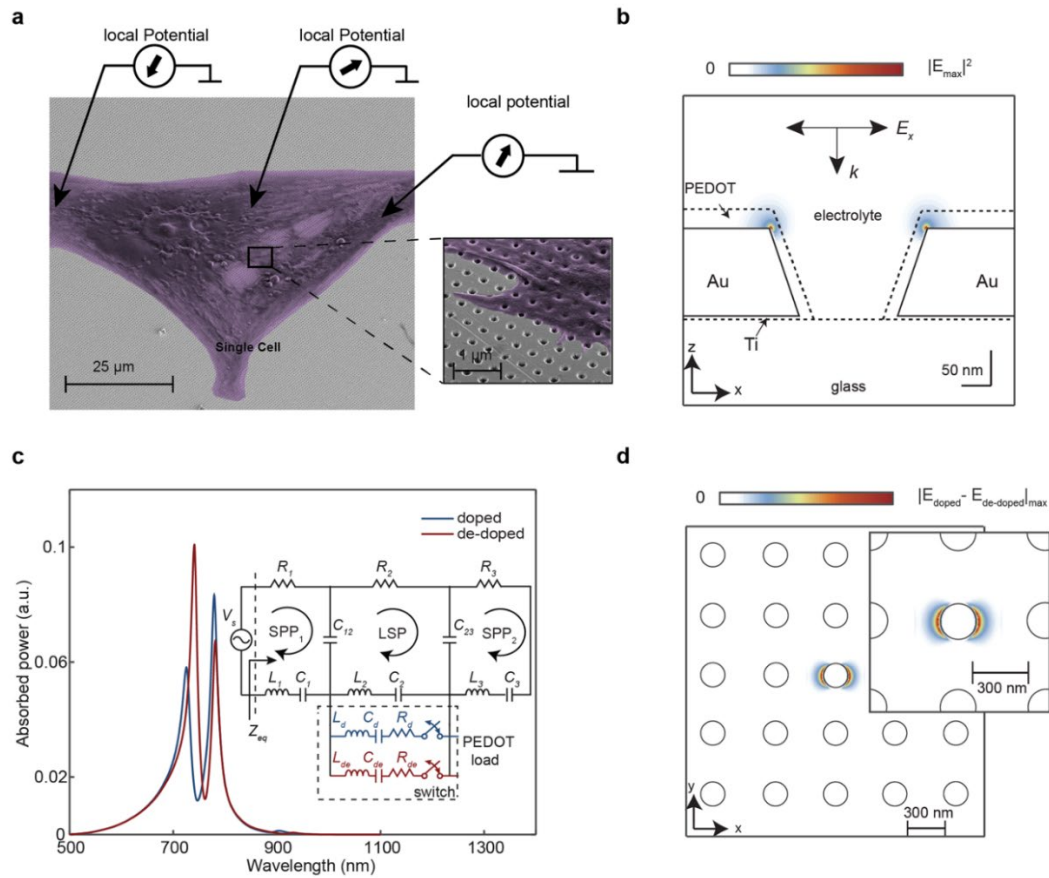


Figure 3.2. Wireless Imaging System. **a.** Scanning electron microscopy image of a single CM on W-NEA. In the inset, enlarged SEM image of CM on a portion of W-NEA shows the considerable size difference between the W-NEA and electrogenic cells. **b.** FDTD simulations the W-NEA indicates strong light confinement within the 25 nm thick PEDOT layer. **c.** Effect of doping (blue curve) and de-doping (red curve) of the PEDOT layer on the transmission spectra of W-NEA. Inset shows the circuit model to explain the intensity modulation of the EOT spectrum. **d.** FDTD simulation of a 5x5 wireless nanoelectrode array demonstrating how a single nanohole operates as a wireless nanoelectrode. These are the same nanoholes as pictured in Figure 3.1b captured in the plane of the gold surface. PEDOT was doped only around the central nanohole and it exhibited increased light transmission and field confinement compared to fully de-doped nanoholes, whereas surrounding nanoholes did not.

3.1.3. Simulating W-NEA Spectra

The W-NEA was modeled using a full-wave FDTD solver provided by Lumerical Inc.

The dielectric constants “Au (Gold)–CRC” were used in gold structures¹⁰⁸. The

complex dielectric constants of PEDOT-PF₆ load were obtained from a previous study¹⁰⁹ using Kramers-Kronig relationship. Symmetric and anti-symmetric boundary conditions were used along y and x direction respectively to minimize the computation time. In the z-direction, perfectly matched layer boundary conditions were used. A linearly polarized excitation source (400 to 1000 nm) was used in our simulations.

3.1.4. Simulating W-NEA Resolution

Each nanohole of W-NEA can function as an optical sensor, resulting in nanoscale resolution electric field imaging. To verify this, we used FDTD simulations to calculate near-field of differently doped nanoelectrode using a 5×5 W-NEA with periodic boundary conditions. We compared field profiles for the array of nanoelectrodes when it is completely undoped and when only the central electrode experiences local doping. The difference is shown in Figure 3.1d where virtually no change was seen by other nanoholes but a strong increase in field concentration is seen for the doped nanoelectrode. The same pattern occurs with near-field transmission in the W-NEA as higher intensity is seen through the doped nanoelectrode and little to no change is seen in others. Therefore, our results confirm that each electrochromically loaded nanohole as an individual nanoelectrode.

3.2. Characterizing W-NEAs

In order to measure a signal with an adequate signal-to-shot-noise ratio (SSNR), electrophysiological imaging technology must address two problems: electric field sensitivity, S_E , and the number of photons detected, N , $SSNR \propto S_E \sqrt{N}$ ³⁴. In previous work, we addressed these two problems by introducing a novel electro-plasmonic

mechanism in which an electrochromically loaded nanoantenna translates local electric field variation to an optical signal with an unprecedented SSNR ~ 200 due to high sensitivity and a remarkably high number of photon counts¹¹⁰. The electrochromic load translates the dynamics of the local electrical field into the variation of the electromagnetic resonance due to the modulation of the equivalent optical impedance, Z_{load} "seen" by the plasmonic resonator with the equivalent optical impedance of Z_{pnr} . However, nanohole based plasmonic resonators are more sensitive to the change in the load compared to the nanoantenna systems because of increased sensitivity to the surroundings, nanohole 481 nm /RIU vs. nanoantenna 167-327 nm/RIU¹¹⁰.

3.2.1. Measuring Sensitivity

To confirm the high field sensitivity, we conducted spectroelectrochemical measurements in a three-electrode configuration and 1x PBS electrolyte solution. We used W-NEA as the working electrode and a platinum counter electrode and Ag/AgCl reference electrode. In our experiments, the zero-bias transmission signal (T_0) and the electric field induced change in the transmission, ΔT , are monitored to obtain differential transmission signals, $\Delta T/T_0$. We have demonstrated that $\Delta T/T_0$ increases linearly with applied potential at a rate of $\Delta T/T_0 = 5 \times 10^{-4} \text{ mv}^{-1}$.

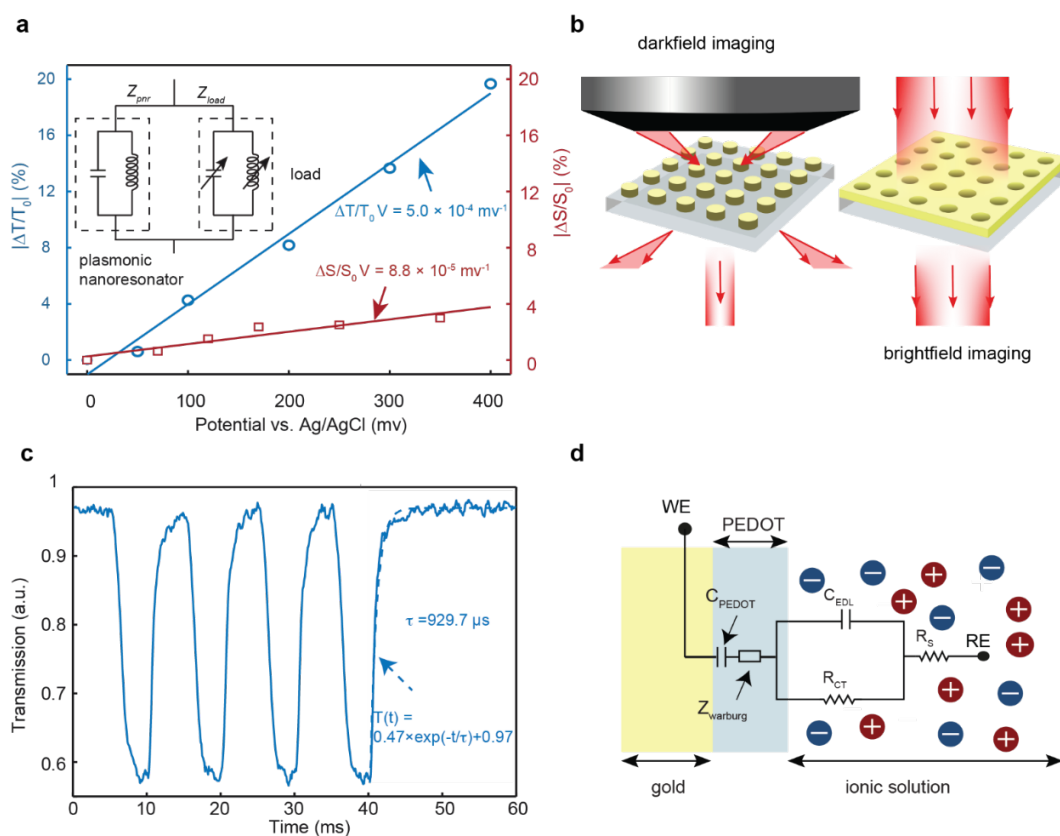


Figure 3.3. Electrochromic loading effect on gold nanoholes. **a.** Electric field sensitivity to the differential transmission signal for W-NEA and nanoantennae array in 1x PBS. The inset shows the schematic of the plasmonic resonator loaded with the electrochromic polymer representing nanoantennae. **b.** Diagram comparison of darkfield imaging a nanoantennae array and brightfield imaging a W-NEA. **c.** Transmission switching of W-NEA recorded in ionic solution in three-electrode spectroelectrochemical cell. A square wave potential alternating between -500 mV and 500 mV versus Ag/AgCl was applied to the working electrode with a potentiostat. Transmitted signals through W-NEA were recorded with a spectrometer with an integration time of 10 ms. **d.** Equivalent circuit model of gold-PEDOT-electrolyte system. In this equivalent circuit, a solution resistance R_s is added in series with an electrolyte-polymer interface element consisting of an electrical double layer (non-faradic) capacitance C_{EDL} and a charge transfer resistance R_{CT} . The bulk redox capacitances of the electrochromic polymer are incorporated into this circuit in series by means of the electronic bulk capacitance C_{PEDOT} and finite-length Warburg diffusion impedance $Z_{Warburg}$, which is characterized by the diffusional pseudocapacitance C_D .

We demonstrated large transmission intensity changes up to 20% for potential values up to 400 mV. Our results compare favorably with those of the electro-plasmonic nanoantenna probes (Figure 3.2a), which provide <3% change in the differential scattering signal with a rate of $\Delta T/T_0 = 8.8 \times 10^{-5} \text{ mV}^{-1}$. Furthermore, W-NEAs have a higher photon throughput and can thus be used to image the activity of a single cell that is lying on a few tens of nanoelectrodes in W-NEA and changes the light transmission when depolarized. W-NEAs employed bight field microscopy, where collimated light from the microscope condenser incident on the sample with high angle approximately at 90 degrees from the imaging surface (Figure 3.2b right panel). If a microscope objective collects the light transmitted though the W-NEA, we see that most of the light would be collected into the objective. On the other hand, in electro-plasmonic nanoantenna employed transmission darkfield microscopy where specialized condenser contains a patch stop filter that blocks direct collimated light from the light source (Figure 3.2b left panel). Light that comes at low- incident angle approximately at 45 degrees from the imaging surface. We can clearly see that most of the light scattered away from the microscope objective and is therefore not collected and suffers from low light throughput and insufficient imaging capacity for at scale electrophysiological imaging. Due to the high sensitivity and photon throughput W-NEA could reliably translate electrophysiological activity from a single cell while maintaining parallel detection of many cells.

3.2.2. Electro-optic characterization of W-NEA

In Air

We developed a system containing the W-NEA without any electrogenic cell to measure the sensitivity of the W-NEA in presence of the applied electric field. The two-electrode parallel plate like system was composed of the W-NEA (bare or loaded) as the bottom electrode, and a transparent ITO-coated (Structure Probe Inc., 06401-CF) as the bottom electrode. The electrodes were separated and filled with air by a 100 μm thick double sided kapton polyimide tape (Ted Pella Inc., 16092-12). The electric potential difference (electric field) applied between the two electrodes was controlled using a power supply (TTi, PLH 250). The far-field transmission signal of the W-NEA (bare or loaded) was obtained by the nikon eclipse Ti-E inverted microscope. The collimated light from the 100 W halogen light source illuminated the W-NEA (from gold side for bare and PEDOT-PF6 for loaded) and the transmitted light was collected by a microscope objective (4x; NA 0.2) and fed into the fiber coupled spectrometer (Ocean optics, HR4000) using custom built collection optics.

In PBS

A custom-built electrochemical cell, consisting of a Pt wire acting as counter electrode, and Ag/AgCl wire as reference electrode, was used for all optoelectrochemical measurements. Electrochemical potential of the W-NEA working electrode was controlled with the Gamry potentiostat by means of potential step voltammetry. 1x PBS solution containing 137 mM sodium chloride (NaCl), 2.7 mM potassium chloride (KCl), 10 mM disodium hydrogen phosphate (Na_2SO_4), and 1.8 mM potassium

dihydrogen phosphate (KH_2PO_4) was used in the experiments with ionic solutions. For the experiments with ion-free solution high purity DI solution was used. The W-NEA surface was illuminated by the collimated light from the halogen light source and a 4x objective captured the transmitted light. The light was then fed into a spectrometer with an integration time of (Ocean Optics, HR4000).

3.2.3. Temporal Response

An imaging system should also have a high temporal response (~ 1 ms) to accurately resolve biological signals. To demonstrate the sub-millisecond switching capability of W-NEA we perform spectroelectrochemical experiments. Collimated light from a LED illuminates the W-NEA. We apply a 100 Hz square wave potential oscillating between +500 mV to 1000 mV vs. Ag/AgCl to W-NEA. The following change in light transmission are collected using a 10-x microscope objective and sent to a photodiode connected to a data acquisition device for capture of data. Our results confirm that W-NEA can follow incident square wave signal and temporal response time of ~ 930 μs (Figure 3.2c). W-NEAs take advantage of unprecedented light electrochromic polymer interaction enabled by plasmonic excitations to achieve fast switching. To get a qualitative understanding of this fast response time, we map our electrochemical system with an equivalent circuit consisting of solution resistance R_{sol} , PEDOT layer electronic bulk capacitance C_{PEDOT} , finite-length Warburg diffusion impedance Z_{Warburg} , charge transfer resistance R_{CT} , and a constant phase element Z_{CPE} . Typically, electrochromic polymers temporal response time scales with thickness of the polymer as it determines the values C_{PEDOT} and the Warburg diffusion impedance Z_{Warburg} .

Conventionally, thickness of the polymer layer needs to be larger to get sizeable change upon modulation; however, this results in a poor RC time constant due to elevated capacitances¹¹¹. Incorporation of electrochromic polymer with the plasmonic negates this requirement and hence an ultrathin layer of polymer can be used, offering a temporal response in the sub-millisecond range. As a result, W-NEA can acquire images at rates greater than 1 kHz using a bright-field imaging system that includes a fast-imaging device, such as high-speed sCMOS cameras.

3.3. High-throughput Electrophysiology with Cardiomyocytes

We use a transmitted light imaging approach based on an inverted microscope provide brightfield illumination to demonstrate high spatial resolution and high throughput electrophysiological imaging (Figure 3.3a left panel). We place the W-NEA in the illumination path to enable electrophysiological imaging (Figure 3.3a left panel-inset). To demonstrate that electrical activity of cells can readily be recorded by our approach, we culture neonatal rat ventricular CMs¹¹² on a W-NEA substrate at a cell density of 31378 cells/mm². We record the electrical activity approximately 1 week from the first day of culture. The optical path of the microscope shown in Figure 3a-right panel, which includes a LED light source (Thorlabs, M700L4) and a sCMOS camera (Hamamatsu, ORCA- Flash 4.0) mounted around a ‘Zeiss Axio Observer’ microscope. The collimated LED light source illuminates the W-NEA and light is transmitted through the subwavelength holes by EOT effect. The transmitted signal is obtained on the exit surface of the W-NEA by the 5x numerical aperture (NA) 0.12 objective and is projected on the full frame of the sCMOS camera (2048 × 2048 pixels) (Figure 3.3a

right panel). The field of view (FOV) is $2662.4 \times 2662.4 \mu\text{m}^2$ in the W-NEA sample plane, corresponding to a magnification of 5x onto the camera. Camera pixel is $1.3 \mu\text{m}$ wide in the W-NEA sample plane ($6.5 \mu\text{m}$ camera plane). As shown in Figure 3b the approach relies on the change in the optical properties of the PEDOT-PF₆ loading at the W-NEA for acquiring electrophysiological images from which pixels activity can be extracted and reconstructed in real-time. Fast acquisition of extracellular electrophysiological signals is performed as a sequence of frames (30 fps) by encoding extracellular voltage signals as pixels data. By using a false color map, this enables video rate observation of the overall network activity as well as the local activity by looking at the intensity change of the pixels.

3.3.1. Results

Figure 3.3c provides electrical activity of a single CM. Single cell spiking data is reconstructed by combining pixels data from sequential. Some cells were manually identified through matching correlated spiking signals in pixel intensity modulation and cell body outlines to produce single cell spiking traces. Pixels covered by the cell area were summed in each frame and the result was bandpass filtered (see methods) to demonstrate spiking behavior. Similar image processing techniques can be applied to monitor the electrical activity of every cell in the FOV. We use blebbistatin (myosin II inhibitor), widely used in cardiac electrophysiology, to prevent motion artifacts triggered by CMs contraction¹¹³. By using fast Ca²⁺ imaging, we confirm that blebbistatin does not interfere with the electrophysiological activity of cells both prior to and after an electro-plasmonic measurement.

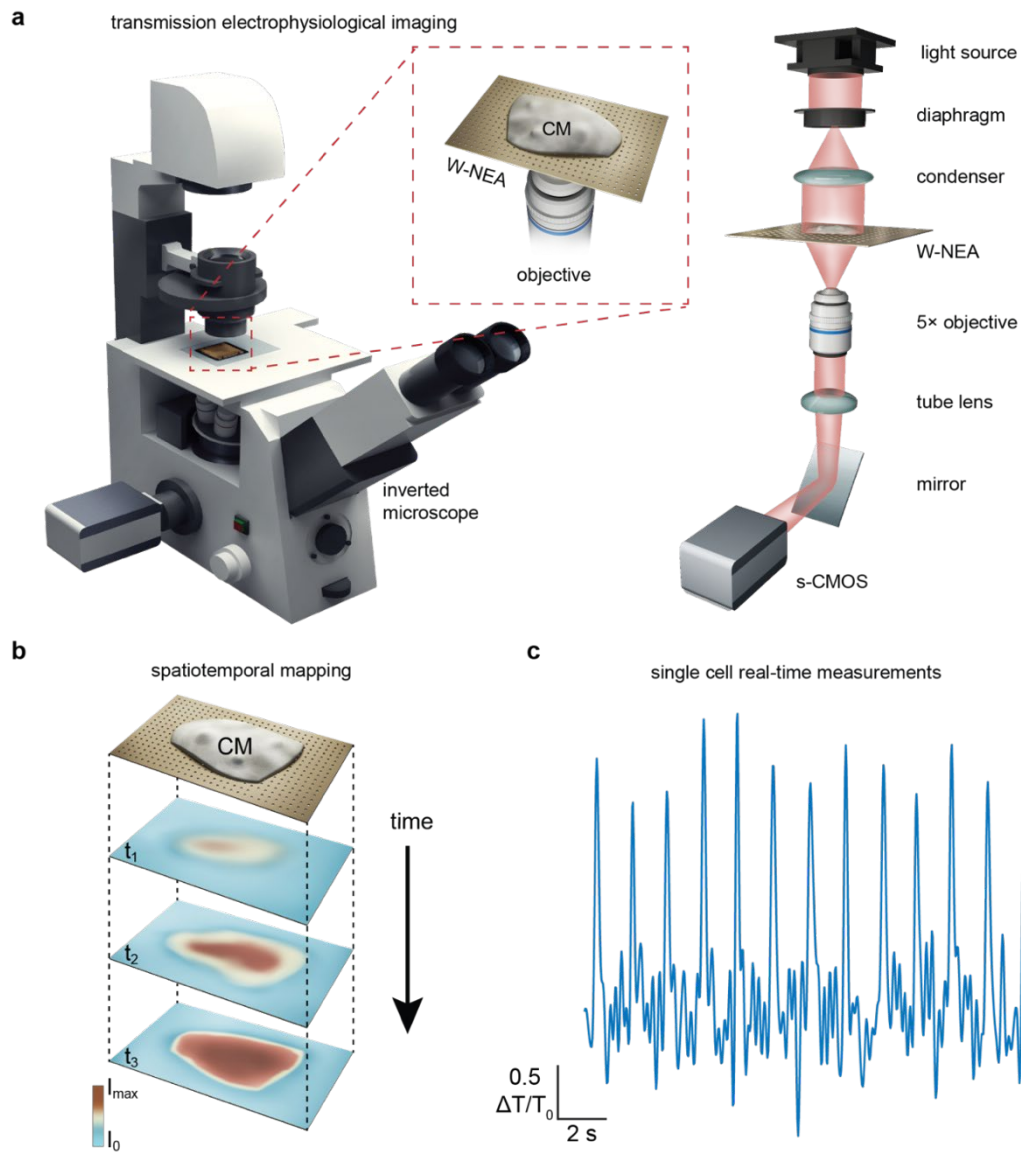


Figure 3.4. Cellular voltage imaging potential. **a.** Experimental schematic showing key components. An LED source illuminates an electrogenic sample on a W-NEA substrate. Transient electric field during cellular firing events modulates the transmission intensity of the W-NEA and an sCMOS camera captures the result. **b.** Frames of a single cell combine to show electric field dynamics with high resolution. **c.** Optical recording of spiking from a single cell on a W-NEA. Pixels within a cell body outline were summed and filtered (see methods) to show single cell intensity changes.

The high spatial resolution W-NEA enables imaging electrical activity of thousands of cells with single cell resolution. To confirm this, the processed contrast adjusted images of CMs cultured on W-NEA are given a spatial Gaussian average and moving average in time (see Methods) to reveal the activity of thousands of cardiomyocytes. Figure 3.4 shows the synchronous beating of CMs in frames at different times. Many CMs are simultaneously activated during a depolarization event, resulting in increased intensity (hot spots). Using the same images, we apply a temporal bandpass filter and bicubic interpolation between pixels in smaller regions to highlight single cell electrical activity. In the insets of Figure 3.4, we show the electrical activity of a single cell cardiomyocyte illustrating the high-resolution capability of our W-NEA. The single cell is easily identified and localized owing to the spatial resolution (nanoscale; 3-order of magnitude smaller than a typical CM). The footprint of the hot spots has a diameter of 4-5 μm (approximately 3 to 4 pixels). W-NEA compares favorably with state-of-the-art electrophysiological imaging techniques. We recorded spontaneous spiking patterns under continuous illumination using a deep red LED light source (nominal wavelength 700 nm) at a light intensity of $\sim 22 \mu\text{W}/\text{mm}^2$. The light intensity used in our experiment is a million-fold lower intensity than the state-of-the-art optical detection techniques owing to the extremely large SSNR enabled by electro-plasmonics. Compared to MEAs, W-NEA features 3-order of magnitude more parallel electrode in the active sensing area with an unprecedented density of ~ 3 million electrode/ mm^2 and 3-order of magnitude higher spatial resolution (Table 3.1). These enables imaging electrical activity of thousands of cells while maintaining access to single cells.

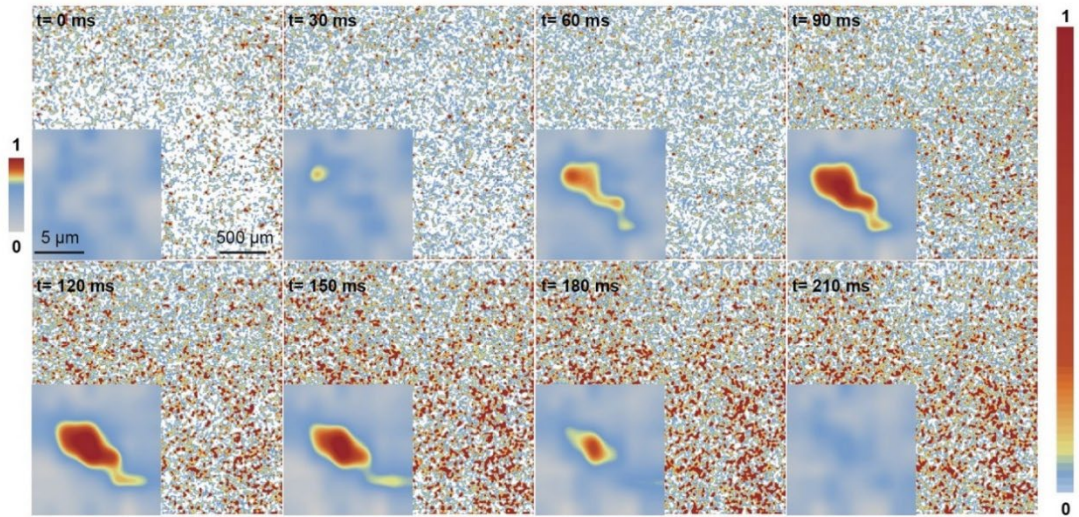


Figure 3.5. Large-scale, high-resolution electrophysiology. Processed images of W-NEA intensity in the full frame (2048×2048 pixels) in response to transient electric field during the cellular firing event of a large number of neonatal rat cardiomyocytes (CMs) with a temporal resolution of 30 ms. Red regions denote clusters of depolarizing CMs. The inset shows a heatmap of a single CM cellular firing event.

Table 3.1. Summary of previously reported high-resolution and high-throughput field probes compared to this work.

Reference	Year of publication	Spatial resolution (μm)	Electrode count	Active area (mm^2)	Electrode density ($/\text{mm}^2$)
Bakkum et al.	2013	17.8	11,011	3.6	3059
Müller et al.	2015	17.5	26,400	8.1	3259
Dragas et al.	2017	13.5	59,760	11	5489
Tsai et al.	2018	25.5	65,536	42.6	1538
This work	-	0.560 (actual) 3 (diffraction limited)	500×10^6	169	3×10^6

3.3.2. Cell Culturing

First W-NEAs were sterilized by immersing in 70% ethanol for 2 hours and air dried under the fume hood. Then substrates were coated with fibronectin ($50 \mu\text{g}/\text{mL}$, Sigma-

Aldrich) and was incubated at 37°C for 30 minutes. Following a phosphate buffered saline (PBS, Corning) wash substrates were seeded with neonatal rat ventricular cardiomyocytes CMs that were isolated according to a previously established protocol¹¹⁴ and following regulations of University of Notre Dame's Institutional Animal Care and Use Committee. Briefly, the hearts were excised from 2-day old neonatal Sprague-Dawley rat pups, diced into small parts, incubated overnight in 0.05% (w/v) Trypsin (Gibco) in Hank's Balanced Salt Solution (HBSS, Gibco) followed by 0.1% collagenase type-2 treatment. All the isolated cells were placed on tissue culture plates. Since heart muscle cells require more time to attach to tissue culture substrate, the first cells attached were heart fibroblasts. Other cells that are present in the heart wall tissue (i.e., endothelial cells) were mostly eliminated due to the specific media used. The unattached cells at the end of the 2-hour pre-plating, mostly heart muscle cells, were collected and seeded onto the W-NEA substrates with a cell density of 1 million cells/mL. The culture was maintained under standard cell culture conditions in Dulbecco's Modified Eagle Medium (DMEM, Hyclone) supplemented with fetal bovine serum (FBS, 10%, Hyclone) and penicillin-streptomycin (P/S, 1%, Corning) with media changes every 3 days.

3.3.3. Immunostaining

These samples were fixed in paraformaldehyde (4%, Electron Microscopy Sciences) for 15 minutes at room temperature, and then washed with PBS. Cells were then permeabilized in Triton X (1%, Sigma-Aldrich) for 15 minutes and then washed with PBS. Cells were blocked with BSA (1%, Sigma-Aldrich) for two hours at room

temperature. After blocking, cells were incubated with mouse monoclonal cardiac Troponin-I (Abcam, CM marker) primary antibody diluted (1:100) in 1% BSA at 4°C overnight. The next day, cells were washed with PBS and then incubated with Alexa Fluor 488 (Life-Technologies) secondary antibody diluted (1:200) in 1% BSA at 4°C for 6 hours. Following the secondary antibody incubation, cells were washed with PBS. The steps were repeated for rabbit monoclonal cardiac Connexin 43 (Abcam, gap junction marker) primary antibodies and Alexa Fluor 594 (Life-Technologies) secondary antibody. After a second staining, cells were incubated with nuclear stain DAPI (1:1000 DAPI: PBS, Sigma Aldrich) and then washed with PBS until no background was seen.

3.3.4. SEM Images

Samples were fixed using 2.5% glutaraldehyde in 0.2 M sodium cacodylate buffer for 2 hours at room temperature. Samples were then placed in DI water for storage and transported to SEM facilities at UCSC. Before imaging, samples were placed in increasing concentrations of ethanol (10%, 25%, 50%, 75%, 90%, 100%) waiting 10 minutes between each placement. Samples subsequently sustained critical point drying in carbon dioxide and immediate sputtering with 10 nm of gold before SEM imaging.

3.3.5. Image Processing

Video was extracted from proprietary CZI files using into MATLAB using Bio-Formats Java API to produce unsigned, 16-bit integer images contained in Motion JPEG 2000 files. Total image intensity was calculated for each video frame and plotted so as to isolate images containing an action potential. Single cell images were produced

by cropping wide field video to only include a single cell and applying slightly different filters. Cut video of an action potential was gaussian blurred using a filter with an 8-pixel standard deviation for wide field and 1-pixel standard deviation for single cell. Each pixel was subsequently time filtered with a five-frame moving average filter for wide field and bandpass filtered for single cell. Single cell bandpass filtering in time utilized 12th order lowpass and 4th order high pass Butterworth filters with 4.5 Hz and 0.15 Hz cutoffs, respectively. To increase image contrast, an image of minimum values for each pixel was generated and subtracted throughout the video. Maxima for all columns in images throughout the video were averaged to yield an adjustment factor, a . For contrast adjustment, all image values were multiplied by $65535/a$ as 65535 is the largest value for unsigned, 16-bit integers. Finally, we applied a custom colormap to images, which were saved as PNG files and compiled into videos.

4. In Vivo Sensing with Electro-plasmonics

In this chapter, I highlight a new research direction in BMIs; we call this technology Neuro-SWARM³ - neurophotonic solution dispersible wireless brain activity reporters for massively multiplex measurements¹¹⁵. Neuro-SWARM³ is a virus-sized electro-plasmonic field probe that can be delivered across the blood-brain barrier with a simple injection. Neuro-SWARM³ provides high signal to shot noise ratio (SSNR $\sim 10^3$) wireless recording capability from single neurons due to its enhanced scattering cross-section and field-sensitivity thanks to electro-plasmonics. Its size and biocompatible electrochromic polymer poly(3,4-ethylenedioxythiophene): polystyrene sulfonate (PEDOT:PSS) coat mean that there is no inflammatory response. Neuro-SWARM³

transmits signals wirelessly using infrared light so neurons can be monitored volumetrically and with massive multiplexing capability. This is an entire system on a nanoparticle as it includes wireless power transfer, electro-optic translation of neural signals, and the broadcasting of those signals. This way, one can utilize the sensitivity that electro-plasmonics offers by making an antenna that translates the electric field to the far-field scattering of light. We envision that Neuro-SWARM³ could have a transformational effect in remote detection of in vivo bioelectric signals, which would be beneficial for brain-machine interface (BMI) innovation.

We introduce a system-on-a-nanoparticle probe, Neuro-SWARM³, enabling non-invasive detection of in vivo electrophysiological activity using near-infrared light. Neuro-SWARM³ converts bioelectric field oscillations to an optically detectable signal that can be picked up from outside the brain using near-infrared (NIR-II, 1000-1700 nm) light. Much like the passive radio frequency identification (RFID) tags, Neuro-SWARM³ reports the spiking activity of cells by modulating the incoming NIR light coupling and the re-radiated light spectrum that is sent back to the reader (detector), a method called backscattering in radio frequency (RF) engineering. Here, the spectrum of the backscattered NIR light is modulated by the electrochromic loading of the plasmonic (electro-plasmonic) nanoantenna, which shows strong sensitivity to the local electric-field dynamics¹⁴. Hence, Neuro-SWARM³ provides a far-field bioelectric signal detection capability in a single nanoparticle device that packs wireless powering, electrophysiological signal detection and data broadcasting capabilities at nanoscale dimensions.

4.1. Neuro-SWARM³

The working principle of Neuro-SWARM³ is summarized in Figure 4.1. In contrast to fNIRS, Neuro-SWARM³ enables direct measurement of the local electric-field dynamics (neural depolarization events) through NIR light. It uses two fundamental mechanisms for electro-optic translation: (1) drastically enhanced light-matter interactions through localized surface plasmon (LSP) excitation, and (2) enhanced electro-optic sensitivity to local electric-field dynamics through the electrochromic loading of poly(3,4-ethylenedioxythiophene): polystyrene sulfonate (PEDOT:PSS)¹⁴. PEDOT:PSS outer layer is biocompatible and do not exhibit cytotoxicity as shown in a previous study focused on rodent cortex¹¹⁶. Furthermore, Neuro-SWARM³, a nanoscale probe that is smaller than 200 nm in diameter, can be functionalized with lipid coatings and injected into the circulatory system to be delivered across the blood-brain barrier via receptor mediated transcytosis¹¹⁷. Figure 4.1a depicts the proposed swarm-and-lock concept schematically. Neuro-SWARM³ are first distributed within the cortical region of the brain and tethered to specific cell membranes through the surface functionalized proteins (Figure 4.1a, inset). Subsequently, far-field scattering signal from the Neuro-SWARM³ is employed to detect the neural activity, the transient electric field oscillations created by the discharging neuron. During a depolarization event, the membrane potential is controlled by the ionic current, that is sodium (Na⁺) and potassium (K⁺) movement through the cell membrane (Figure 4.1b). Large fluctuations in the membrane potential occur as a result of Na⁺ influx into the cell (spike or depolarization phase) and K⁺ efflux from the cell (repolarization phase)⁵⁸.

Such large charge density (ion concentration) perturbations can give rise to strong transient electric fields ($E_{\text{transient}}$). One can estimate the strength of $E_{\text{transient}}$ outside the cellular membrane using a charge transfer model. A neural cell can be treated as a 20 μm diameter spherical lipid bilayer with a specific capacitance ($C_m = 1 \mu\text{F}/\text{cm}^2$)¹¹⁸. For a transmembrane potential variation of $\sim 110 \text{ mV}$ (Figure 4.1b), the total charge that is moved across a cell membrane during a spiking event can be calculated as in $Q = C_m A_{\text{cell}} V_m$. Here, A_{cell} is the total surface area of the cellular membrane, and V_m is the change in the membrane potential. Such a charging event requires 8.6 million monovalent Na^+ ions to rush into the cell during the spiking phase. One can calculate the instantaneous extracellular electric field strength right outside the cell using this extra charge and the dielectric constant ($\epsilon_{\text{CSF}} = 88.9$) of the cerebrospinal fluid. This model, although simple, accurately captures the extracellular field values, which are typically few tens of mV/nm in strength¹¹⁹. Such large extracellular electric-fields can lead to strong modulations in the backscattering signal of Neuro-SWARM³, enabling far-field detection, as illustrated in Figure 4.1c.

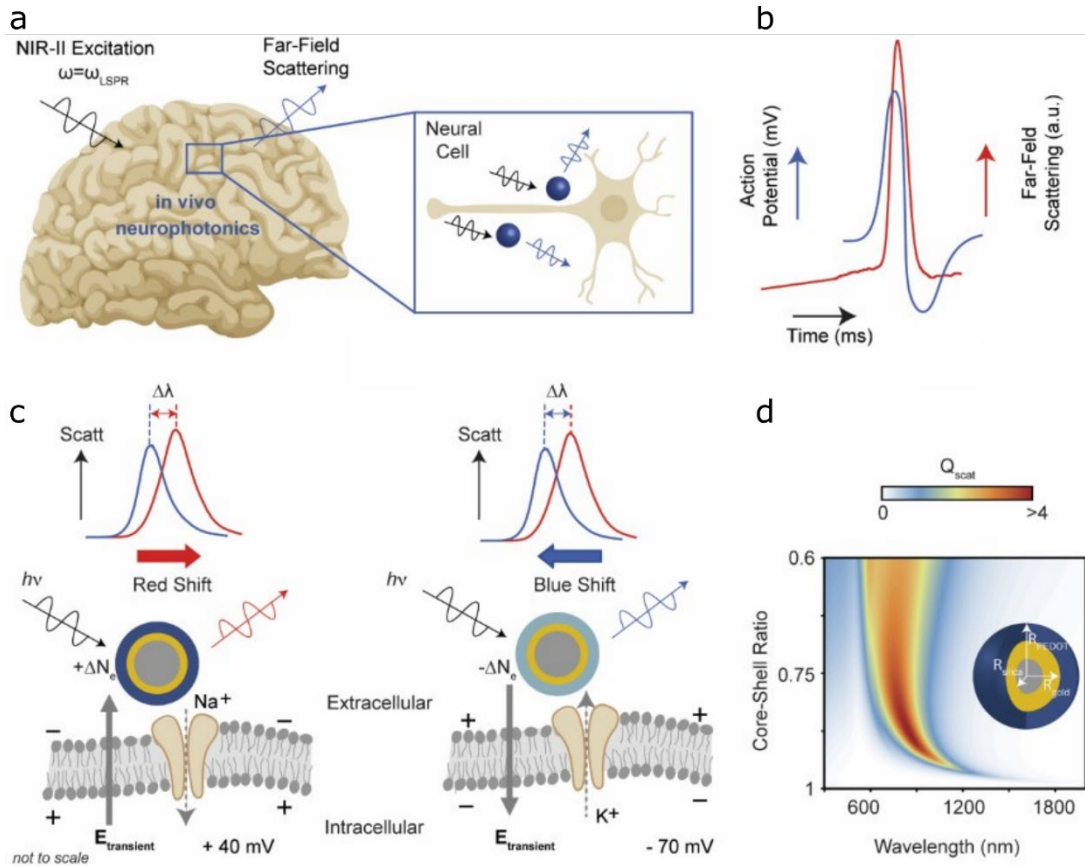


Figure 4.1. Mechanism of Operation. **a.** Neuro-SWARM³ enables remote detection of neural cell activity using NIR-II light far-field scattering. **b.** Cell depolarization (spiking) causes a high transient electric field leading to increased light scattering and red shifting of the electro-plasmonic (electrochromic-plasmonic) nanoantenna resonance spectrum. Return to resting potential (repolarization) results in reversal of the scattering spectrum changes.

4.2. Field Sensitivity

Neuro-SWARM³ (SiO_x core radius of 63 nm, 5 nm thick Au shell) is designed to exhibit plasmonic resonance scattering at 1050 nm, corresponding to a wavelength regime enabling deep tissue penetration¹²⁰. A spherically symmetric structure is chosen to minimize the polarization dependence.

4.2.1. Multisphere Mie Theory and Design

We used Mie theory for the multilayered core-shell structure scattering efficiency calculations^{121,122}. This theory solves for the inward and outward sets of electric and magnetic fields consisting of spherical wave functions. Each layer of the multisphere is defined by a size parameter $k_l = 2\pi n_m r_l / \lambda$ and its relative refractive index $m_l = n_l / n_m$ where l is the layer and n_l is its refractive index. n_m is the refractive index of the medium surrounding the particle, r_l is the outer radius of layer l , and λ is the probing wavelength. Electric and magnetic fields in each layer are described by a complex summation of sinusoids and Riccati-Bessel functions following

$$E_l = \sum_{n=1}^{\infty} E_n \left[c_n^{(1)} M_{o1n}^{(1)} - i d_n^{(1)} N_{e1n}^{(1)} + i a_n^{(1)} N_{e1n}^{(3)} - b_n^{(1)} M_{o1n}^{(3)} \right]$$

$$H_l = \frac{k_l}{\omega \mu} \sum_{n=1}^{\infty} E_n \left[d_n^{(1)} M_{e1n}^{(1)} + i c_n^{(1)} N_{o1n}^{(1)} - i b_n^{(1)} N_{o1n}^{(3)} - a_n^{(1)} M_{e1n}^{(3)} \right]$$

Where M_{o1n} , M_{e1n} , N_{o1n} , and N_{e1n} are vector spherical harmonics and their superscripts denote their kind of Bessel function. $E_n = i^n E_0 (2n + 1) / (n(n + 1))$, E_0 being the magnitude of the incident field, i is the imaginary number, ω is the angular frequency of incoming radiation, and μ is the magnetic susceptibility. Symbols $a_n^{(1)}$, $b_n^{(1)}$, $c_n^{(1)}$, and $d_n^{(1)}$ are expansion coefficients which are solved for by applying the boundary conditions:

$$(E_{l+1} - E_l) \times \hat{e}_r = 0 \text{ and } (H_{l+1} - H_l) \times \hat{e}_r = 0$$

These are then compared to expressions for the incident and scattered fields to solve for the scattering coefficients, a_n^{L+1} and b_n^{L+1} , where L is the number of layers in the particle. Using this theory, we were able to generate the scattering efficiencies of many particle geometries to choose an optimal design. The complexity of these simulations was limited by (1) using a fixed electrochromic polymer thickness and (2) by considering the fact that the spectrum of a simple core-shell plasmonic nanoparticle is dependent on its core-shell ratio¹²³. By mapping the scattering efficiencies of many particle ratios for 300-2000 nm wavelengths (Figure 4.1d) we found a region of high scattering ($Q_{sca} > 4$). High scattering is crucial for attaining high photon counts to minimize shot noise. The extents of this high scattering region were used to select the longest wavelength for probing and the corresponding nanoparticle geometry to use.

4.2.2. Simulating Sensitivity with a Drude Model

After establishing that we can generate scattering efficiencies of multilayered nanoparticles, we sought to investigate the change in this scattering for applied electric fields. In Mie theory, this is determined entirely by the dielectric constant of the conducting polymer load (PEDOT:PSS), which we incorporated using Drude's model¹²⁴. A Drude model describes the dielectric constant of a conducting material as follows:

$$\varepsilon(\omega) = \varepsilon_\infty - \frac{\omega_p^2}{\omega(\omega + i\gamma)}$$

where ω is the angular velocity of light, ε_∞ is the relative permittivity at the high frequency limit, ω_p is the plasma frequency of the material, and γ is the damping

coefficient. An applied electric field modulates the dielectric constant of the material by altering the charge carrier density, N , which ultimately affects the plasma frequency, ω_p . The plasma frequency depends on charge carriers as $\omega_p = \sqrt{e^2 N / \epsilon_0 m}$, where e is electron charge, N is the charge carrier density, ϵ_0 is the vacuum permittivity, and m is the effective mass of the charge carrier (electron)¹²⁵. Considering that the charges on the surface of the electrochromic polymer should mirror the electric field applied to it¹²⁶, the change in surface charge density is $\Delta\sigma = -\epsilon_0 E$. The corresponding modulation in electron density is $\Delta N = -\Delta\sigma / e d_{TF}$ where d_{TF} is the Thomas-Fermi screening length. Using these equations and parameters derived from experimental measurements¹²⁷, we can relate an applied electric field to the dielectric constant of PEDOT:PSS in a multilayered nanoparticle.

Notably, the change in the plasma frequency of PEDOT (and hence the change in its dielectric constant) is much greater than that of metals due to having much smaller charge carrier density. An electric field will change the materials charge carrier density and the change in plasma frequency with respect to charge carrier density is the derivative:

$$\frac{d}{dN} \omega_p = \frac{d}{dN} \sqrt{\frac{e^2 N}{\epsilon_0 m}} = \frac{1}{2} \sqrt{\frac{e^2}{\epsilon_0 m N}} \propto \sqrt{\frac{1}{N}}$$

The charge carrier density in PEDOT is about eight orders of magnitude smaller than that of metals like gold^{125,128}. As a result, a large shift in the Neuro-SWARM³ scattering spectrum can be seen with relatively small electric fields (Figure 4.2a). In comparison,

quantum dots report electric fields via the quantum confined Stark effect, which is relatively weak. Based on this effect, fluorescence is directly proportional to changes in the fluorescent lifetime, and the same electric field applied to QDs will produce almost half the optical response than if it were applied to Neuro-SWARM³ (Figure 4.2b)³⁶.

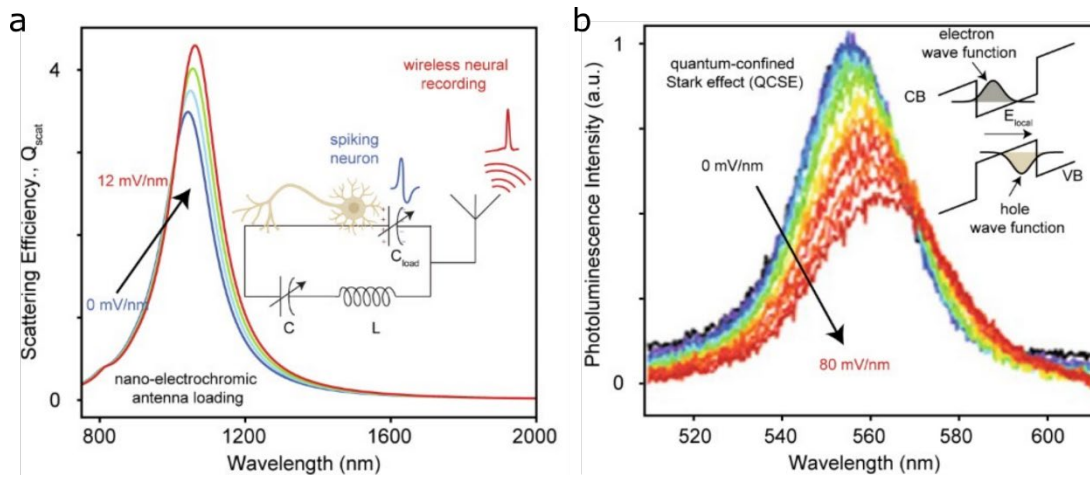


Figure 4.2. Sensitivity comparison. **a.** Optical scattering efficiency, Q_{scat} , spectra for silica-gold nanoshells loaded with PEDOT: PSS. Electric field dependence is shown for 0-12 mV/nm with increments of 4 mV/nm. A core-shell nanoparticle with 63 nm silica core radius, 5 nm thick gold shell, and 15 nm thick PEDOT: PSS coating is considered. Inset shows an equivalent “lumped” optical nanocircuit model of the Neuro-SWARM³. Local electric-field signal (cell spiking) is translated to the nanoantenna backscattering spectrum through the capacitive (PEDOT:PSS) loading effects. **b.** Electric field dependent change in quantum dot (QD) fluorescence based on the quantum-confined Stark effect (inset). Here QDs require an electric field nearly twice as strong for the same modulation in optical response³⁶.

4.2.3. Optimizing PEDOT Thickness

Electro-optic response of the conducting polymer is incorporated using a similar approach detailed in an earlier work on lithographically fabricated in vitro electro-plasmonic nanoantenna¹⁴. Briefly, a plasma frequency modulation of $\Delta\omega_p = (\omega_p/2N) \times$

N is assumed for the dielectric load, where N is the surface charge density variation due to a transient extracellular electric field. Such an analytical treatment of the PEDOT:PSS load was validated in an earlier experimental *in vitro* study using visible light and cultured electrogenic cells¹⁴. In this letter, unlike *in vitro* electro-plasmonic probes, the Neuro-SWARM³ is designed as a colloidal core-shell electro-plasmonic structure for (i) operability at the NIR frequencies and (ii) non-invasive far-field detection of the *in vivo* electrophysiological signals. We calculated the scattering efficiency for electric field strengths ranging from 0 mV/nm to 12 mV/nm with increments of 4 mV/nm (Fig. 2). Neuro-SWARM³ demonstrated a scattering efficiency modulation over 20% for an electric field of 12 mV/nm at LSP resonance wavelength at ~ 1050 nm.

Electro-optic modulation up to $\sim 40\%$ is also observed at off-resonance wavelengths (~ 1200 nm), albeit with a lower photon count signal. Electro-optic response of the Neuro-SWARM³ can be understood following a lumped optical nanocircuit model for the electrochromic polymer (PEDOT:PSS)-nanoantenna system. The electrochromic load, acting as an electric field-controlled nano-capacitor, C_{load} , translates the extracellular electric-field dynamics to a scattering signal modulation, as shown in Figure 4.2a inset. We analyzed the scattering signal dependence on PEDOT:PSS layer thickness (Figure 4.3a). Conventionally, thicker electrochromic films are needed to achieve a strong electro-optic differential signal, which leads to slower temporal response. Neuro-SWARM³ realizes faster response times and strong signal modulations simultaneously using enhanced light-matter interactions in nanoscale

electromagnetic ‘hotspots’ around the plasmonic core-shell structure (Fig. 4.3 bottom right inset). In an earlier work, we experimentally demonstrated that sub-millisecond switching times down to $\sim 200 \mu\text{s}$ are achievable using a $\sim 20 \text{ nm}$ thick PEDOT layer on lithographically fabricated electro-plasmonic nanodisk antenna¹⁴.

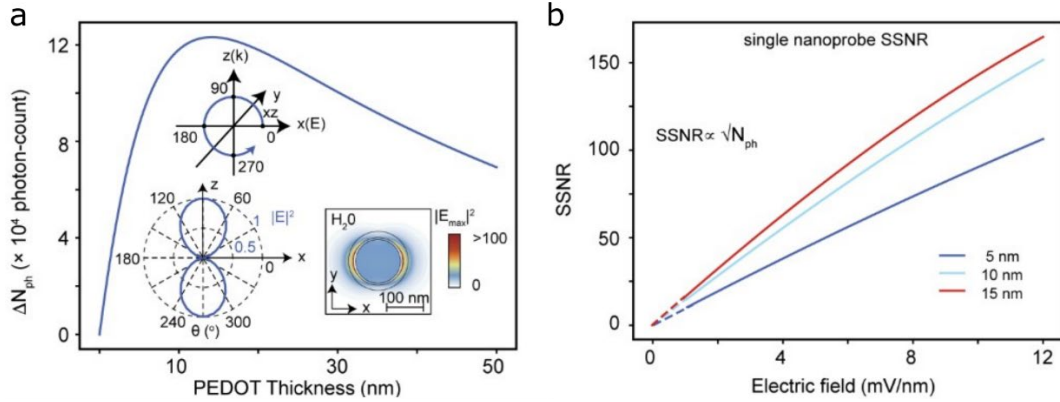


Figure 4.3. Effects of adding an electrochromic polymer **a.** Differential scattering signal for Neuro-SWARM³ with varying PEDOT:PSS load thickness. The polar plot of the angular scattering by the nanoprobe for linearly polarized incident light (1050 nm) in the x direction is shown in the bottom left (inset). The top inset illustrates how the scattering angle is defined within the xz plane. Electromagnetic ‘hotspots’ due to plasmonic hotspots at 1050 nm are shown in the bottom right (inset). Finite difference time domain (FDTD) calculations were employed to calculate angular scattering and cross-sectional field profile. **b.** The SSNR of Neuro-SWARM³ improves with added PEDOT thickness up to $\sim 15 \text{ nm}$ which matches Figure 4.3a. Notably, the sensor response is very linear regardless of electrochromic thickness.

In a typical optical system, the differential optical signal (photon count) can be calculated as in $N_{ph} = I_{inc}(\Delta Q_{sca} \pi r^2)(\lambda/hc)\eta T t_{int}$ where Q_{sca} is the change in the scattering cross section, I_{inc} is the incident light intensity (10 mW/mm^2), η is the solid angle fraction of the total scattered light collected by a microscope objective (assuming a $20\times$ obj., $NA = 0.9$)¹²⁹, T is the detection efficiency (quantum yield 0.5), t_{int} is the integration time (1 ms), c is the speed of light, h is Planck’s constant, r is the radius of

Neuro-SWARM³, and λ is the probing wavelength. As shown in Figure 4.3a, a single Neuro-SWARM³ particle loaded with a thin layer of 5-20 nm PEDOT:PSS can generate a large differential signal (~ 120 k photons) that can be readily detected. Decreasing scattering signal with increasing PEDOT:PSS thickness beyond ~ 20 nm is due to the de-tuning of the electro-plasmonic resonance and probing wavelength (1050 nm) with increasing dielectric loading.

4.3. Modeling Neural Sensing

4.3.1. Biological Neural Activity

We demonstrated the functionality of the Neuro-SWARM³ for label-free optical detection of depolarization events using an Izhikevich model for a neuron. Constant voltage pulses (1 mV, 10 ms) were provided as an input at pseudo-random times such that inputs averaged 10 Hz, and model parameters were set such that the neuron exhibits phasic spiking (Figure 4.4, black)¹³⁰. Results were generated in 0.1 ms steps and data was compressed by taking the maximum every ten points to preserve relative spike amplitudes for 1 ms integration times. This model was chosen both because of its simplicity and its ability to recreate complex neural voltage dynamics that are akin to realistic biology.

4.3.2. Generating Electric Field

The extracellular field is largely determined by the flow of ions across the cell membrane during spiking. At rest, ionic layer around the membrane surface screens nearly all electric field. However, strong transient electric fields are created during the

depolarization and repolarization events as discussed in section 4.1. As the cell membrane acts as a (dis)charging capacitor, we approximate this field by taking the derivative of membrane voltage with respect to time $I \propto dV/dt$ and adjusting the amplitude of the resulting field to 3 mV/nm, a conservative maximum field estimate according to a previous study¹¹⁹.

4.3.3. Comparison with Quantum Dots

In Fig. 4.4, we compared the Neuro-SWARM³ differential signal with that of CdSe quantum dots (QDs), which have recently received significant attention as high photon count alternatives to GEVIs¹³¹. Differential fluorescence provided by a QD due to an external electric field can be expressed as in $\Delta F/F_0 = -\Delta\tau_r/\tau_r(1 - \Phi)$, where $\Phi = 0.5$ is the quantum efficiency and $\Delta\tau_r/\tau_r = 0.5\%$ is the percentage change in the fluorescence lifetime of the decaying excitations. QDs (1.2 nm² cross section) are illuminated with 100 mW/mm² visible light (650 nm)⁶⁴.

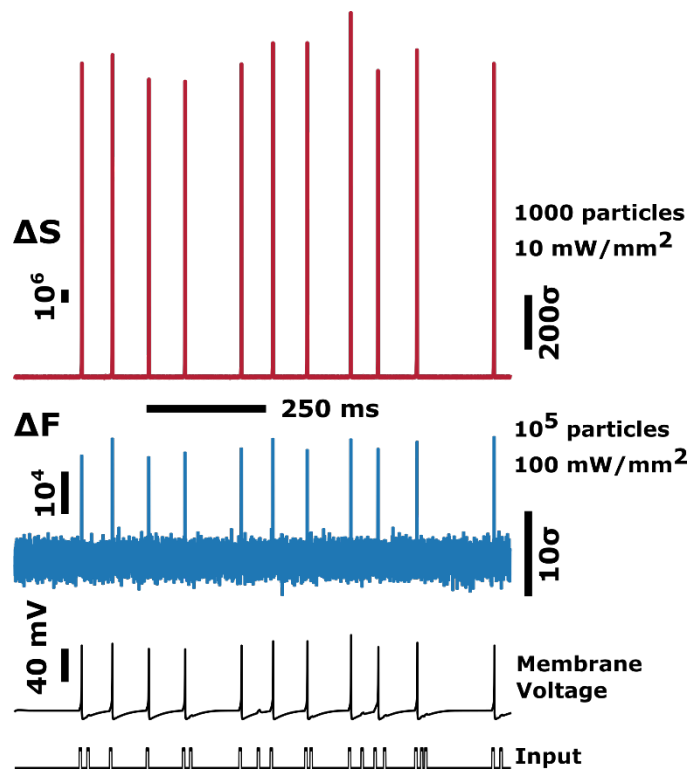


Figure 4.4. Simulated electrophysiological recordings with Neuro-SWARM³ and quantum dots (QDs). A phasic spiking Izhikevich model is used for the neural spiking activity at pseudo-random times. The input and resulting membrane voltage are shown (bottom, black). Differential scattering signal detected from 10^3 Neuro-SWARM³ probes (red, top) is shown assuming a light intensity of 10 mW/mm^2 at 1050 nm . Differential fluorescence signal obtained from 10^5 CdSe quantum dots is compared for an illumination intensity of 100 mW/mm^2 (middle, blue). A maximum extracellular field of 3 mV/nm is assumed. Scales indicating the photon count for the differential signal and the standard deviation due to the shot noise are shown on the left and right, respectively.

Resulting traces show that individual Neuro-SWARM³ probes (Figure 4.4, red) readily outperform QDs (Figure 4.4, blue) by providing at least four orders of magnitude enhanced photon count measurements (left axis), despite the use of 10-fold reduced light intensity (10 mW/mm^2). The fundamental detection limit to any optical measurement technique is the shot noise limit $\text{SSNR} \sim (S/S_0)\sqrt{N_{\text{ph}}}$, where S/S_0 is the differential scattering signal and N_{ph} is the photon count. As show in Fig. 4.4, a

remarkably high SSNR measurement capability (SSNR $\sim 10^3$) is achieved due to drastically higher photon-count signals obtained from the Neuro-SWARM³ (right axis).

4.4. Utilizing a Magnetic Core

We can take this technology a step further by granting it magnetic properties. By replacing the SiO_x core of Neuro-SWARM³ with magnetite (Fe₃O₄), we can gain additional abilities that were not possible using a purely dielectric core. This includes the ability to stimulate neurons using magnetothermal stimulation and the ability to direct nanoparticles to regions of interest using external magnets.

4.4.1. Magnetothermal Stimulation

Magnetic nanoparticles (MNPs) have been used to induce neural spiking via magnetothermal stimulation¹³²; this mechanism can be incorporated into Neuro-SWARM³ to make it a bidirectional BMI. By applying an alternating magnetic field to MNPs, magnetic dipoles oscillate rapidly to align with this field, which generates heat in a process known as Neel relaxation¹³³. Heat sensitive TRPV1 ion channels, common in neurons throughout the brain, increase calcium permeability in response to an increase in temperature above 43 °C, which triggers an action potential (Figure 4.5a)¹³². Using this method, magnets external to a subject could direct alternating fields through the skull to heat particles and trigger magnetothermal stimulation of targeted regions of the brain.

To further investigate the ability of a multilayered nanoparticle to execute this task, we constructed multiphysics simulations to compare temperature profiles

generated by layered nanoparticles. We constructed simulations for bare MNPs, biocompatible Dextran coated MNPs, and a magnetic Neuro-SWARM³ nanoparticle. Since the only magnetic material is the magnetite core, we assume that each core is the same size (80 nm) and generates the same power output.

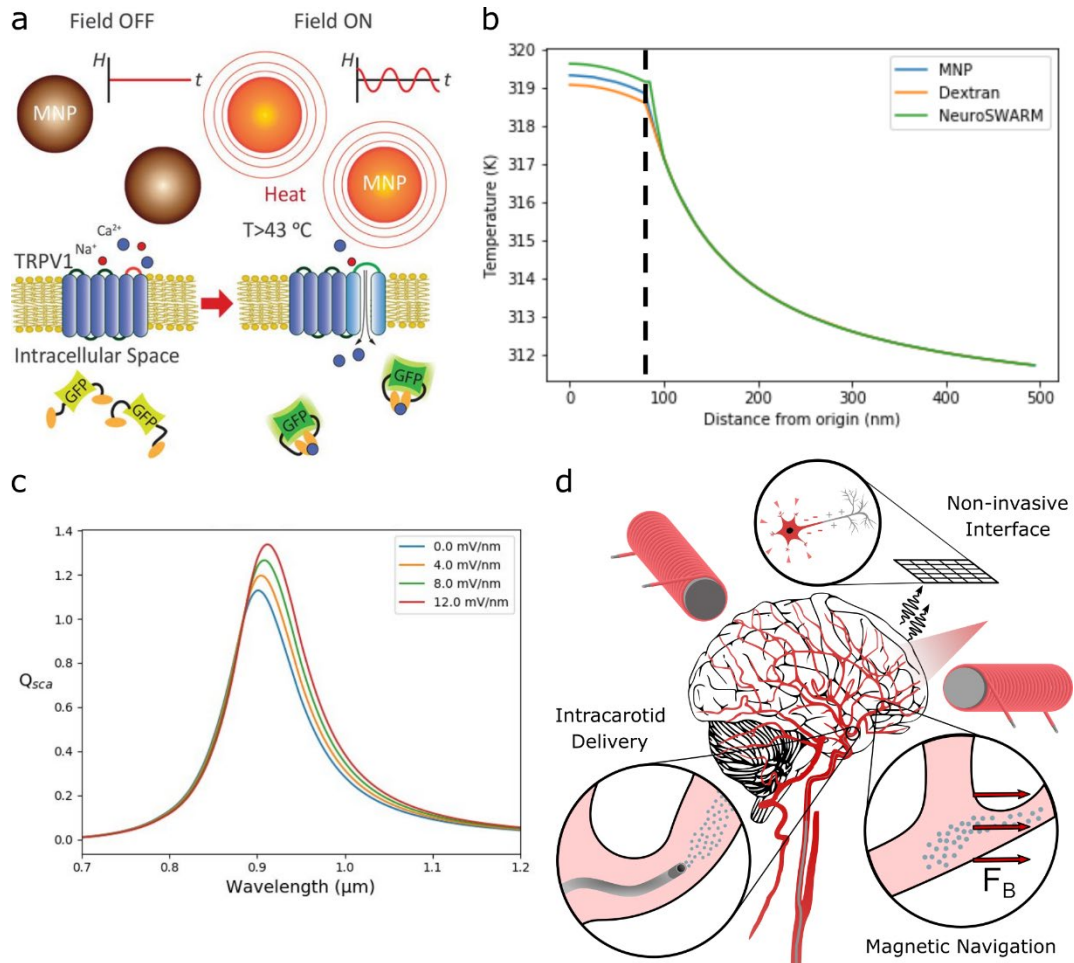


Figure 4.5. A Magnetic Neuro-SWARM³. **a.** The principal mechanism of magnetothermal stimulation¹³². **b.** The result of multiphysics simulations demonstrating nearly identical thermal output. **c.** Scattering spectra of magnetic Neuro-SWARM³ particles under different applied electric fields. **d.** Summary illustration showing intracarotid delivery, magnetic navigation, and non-invasive recording.

We collected information on the heat capacity^{134–136} and thermal conductivity^{137–139} of materials used in the simulation, and employed heat transfer physics¹⁴⁰ in COMSOL to generate a steady state temperature profile from each nanoparticle as seen in Figure 4.5b. The black, dashed line is the radius of the magnetite core, and it is evident that the temperature profiles of all three particles converge almost immediately outside of their coatings. Intuitively this makes sense as the thermal output power from each particle is the same and internal temperature differences are caused by differences in heat capacity. This verifies that a magnetic Neuro-SWARM³ can deliver magnetothermal stimulation just as well as MNPs.

In using a new core material in Neuro-SWARM³, the monitoring abilities of the probe are affected, but sensitivity is maintained. The optical properties of magnetite¹⁴¹ were used to generate scattering spectra of a magnetic Neuro-SWARM³ (Figure 4.5c). The overall scattering efficiency is considerably decreased, which means less light will be reflected for monitoring and measurements will have more noise. However, the magnetic probe still maintains a value over unity, which still amounts to a cross-section that is four orders of magnitude larger than that of QDs⁶⁴. Additionally, high sensitivity is retained in the magnetic Neuro-SWARM³ at ~1% per mV/nm. Hence, a magnetic Neuro-SWARM³ makes for a viable bidirectional brain-machine interface with the trade-off being somewhat more noise during recording.

4.4.2. Delivery and Navigation

Delivery of therapeutics and contrast agents to the brain can pose significant challenges¹⁴². The brain maintains a tightly regulated boundary known as the blood-

brain barrier (BBB) which safeguards the brain. This barrier is made up of endothelial cells, pericytes, and several other kinds of cells along with a slew of transporters, receptors, and other junction proteins that makes it notoriously difficult for therapeutics to reach the brain¹⁴³. The uptake of materials through the BBB has several avenues; some small water-soluble compounds may make it through tight junctions, lipid-soluble materials may diffuse through endothelial membranes, and important nutrients like glucose, amino acids, and other proteins have corresponding transport proteins to traverse the barrier¹⁴⁴. Molecules with specialized receptors or surface charge can also induce cellular endocytosis to circumvent safeguards, and strategies in neuro-nanomedicine have been developed to take advantage of these pathways¹⁴⁵.

Many approaches have been developed for nanoparticles to bypass the therapeutic obstacle that is the BBB¹⁴⁶. Unfunctionalized nanoparticles, that is those without a bioconjugate coating, are limited to being under ~50 nm in order to cross the BBB; however, functionalized nanoparticles over 300 nm can cross the BBB^{145,147}. The polymer coating on Neuro-SWARM³ makes it amenable to functionalization for inducing endocytosis and drastically increasing uptake by the BBB^{148,149}. However, even functionalized nanoparticles are subject to diffusion in the parenchymal space once beyond the BBB, but a magnetic Neuro-SWARM³ has added benefits to enhance targeting.

For a magnetic Neuro-SWARM³, magnetism is also advantageous for magnetic navigation of particles to regions of interest. Using magnetic fields, researchers have been able to enhance the transfer of therapeutics using MNPs not only to specific

regions of the brain but also across the BBB^{150,151}. Scientists performed in vivo studies to show that they could aggregate magnetic nanoparticles to the outermost cortical layers of the brain¹⁵². The same principles can be applied to Neuro-SWARM³ (Figure 4.5d) to create a two-way BMI that can be steered throughout the brain.

4.5. Discussion

Neuro-SWARM³, a system-on-nanoparticle probe, enabling wireless detection of bioelectric signals with single neuron resolution is shown. Neuro-SWARM³ merges wireless power transfer, electrophysiological signal detection and data broadcasting capabilities in a core-shell nanoparticle structure. It offers high SSNR ($\sim 10^3$) measurements from single neurons within the biologically transparent near-infrared window (NIR II 1000-1700 nm) for non-invasive neural recordings through the skull. Neuro-SWARM³ technology can open new horizons for brain-machine interfaces. The integration of Neuro-SWARM³ with functional spectroscopy could lead to an all-optical methodology, allowing simultaneous detection and distinguishing of the fast neuronal signals (Neuro-SWARM³) and the slow hemodynamic activity (fNIRS). However, Neuro-SWARM³ is only a reality in silico, and there are many considerations to be taken into account for the realization of this breakthrough.

The chemistry to produce Neuro-SWARM³ must be developed before testing these devices can begin. Previously, researchers have shown various gold nanostructures coated in the electrochromic polymer, PANI^{153,154}, but ultrathin nanoparticle coatings have yet to be shown with the biocompatible polymer, PEDOT, likely because PANI shows a better electrochromic response¹⁵⁵ and electro-plasmonics

for biological applications have only recently been explored. The first two, core/shell layers of Neuro-SWARM³ are presently sold in industrial quantities with variable thicknesses and high monodispersity¹⁵⁶. Existing chemistry methodologies constructing polymer-coated metallic nanoparticles suggest Neuro-SWARM³ fabrication is feasible¹⁵⁷. However, this remains an uncertainty, and more process adjustments will need to be made upon successful fabrication, especially because the translation of sensitive chemical methods like these do not always easily scale for manufacturing purposes¹⁵⁸.

Like other label-free neural sensing technologies, Neuro-SWARM³ presently lacks the ability to target specific cells and will likely experience difficulty in cellular localization. After breaching the BBB, Neuro-SWARM³ will drift about the extracellular space and, without a binding mechanism, its distance from the cell and the overall distribution of probes will be subject to fluid flow in the brain. This process is much slower than that of action potential dynamics, so artifacts occurring over the course of a minute or longer will be easily distinguishable¹⁵⁹. However, it is critical that a sufficient volume of NeuroSWARM³ particles remain in areas of interest before being eliminated from the body. We can modulate how quickly Neuro-SWARM is flushed out by changing their functional coating to increase or decrease cellular adhesion¹⁶⁰. Moreover, the distribution of nanoparticles amongst themselves is also important. Clustering plasmonic particles have been show to exhibit hybridized spectra¹⁶¹; the impact of spectrum hybridization on the resulting optical signal have yet to be investigated.

Lastly, the toxicity, stability, and target delivery are not yet known for Neuro-SWARM³. PEDOT is known to be a highly biocompatible polymer¹⁶², but of course there is always a limit on how much can be introduced to biological systems before it becomes destructive. Based on previous studies^{116,163}, it is exceedingly unlikely that doses sufficient for monitoring will be toxic, but this is still an important area of research for clinical translation. Moreover, the stability of these particles in vivo is unknown and crucial for operations. It has been shown that nanoparticles made of biocompatible materials can still degrade rapidly in biological environments¹⁶⁴. It has been shown that PEDOT has excellent stability on the scale of weeks¹⁶⁵, but more testing is needed to use Neuro-SWARM³ long-term. Maintaining structure is important not only for operations, but also for toxicity¹⁶⁶ in the case of a magnetic Neuro-SWARM³. NeuroSWARM³ can take advantage of coatings like PEG that boost stability¹⁶⁷, but again, this is an area that warrants exploration. Making Neuro-SWARM³ a reality is well within the realm of possibility, and the avenues of research to precipitate this technology are clear. Despite its infancy, Neuro-SWARM³ and other electro-plasmonic brain-machine interfaces are positioned to change electrophysiology for the better.

Bibliography

1. Verkhatsky, A., Krishtal, O. A. & Petersen, O. H. From Galvani to patch clamp: the development of electrophysiology. *Pflüg. Arch.* **453**, 233–247 (2006).
2. Pine, J. A History of MEA Development. in *Advances in Network Electrophysiology: Using Multi-Electrode Arrays* (eds. Taketani, M. & Baudry, M.) 3–23 (Springer US, 2006). doi:10.1007/0-387-25858-2_1.

3. Stett, A. *et al.* Biological application of microelectrode arrays in drug discovery and basic research. *Anal. Bioanal. Chem.* **377**, 486–495 (2003).
4. Shafer, T. J. Application of Microelectrode Array Approaches to Neurotoxicity Testing and Screening. in *In Vitro Neuronal Networks: From Culturing Methods to Neuro-Technological Applications* (eds. Chiappalone, M., Pasquale, V. & Frega, M.) 275–297 (Springer International Publishing, 2019). doi:10.1007/978-3-030-11135-9_12.
5. Obien, M. E. J., Gong, W., Frey, U. & Bakkum, D. J. CMOS-Based High-Density Microelectrode Arrays: Technology and Applications. in *Emerging Trends in Neuro Engineering and Neural Computation* (eds. Bhatti, A., Lee, K. H., Garmestani, H. & Lim, C. P.) 3–39 (Springer, 2017). doi:10.1007/978-981-10-3957-7_1.
6. Ferguson, M., Sharma, D., Ross, D. & Zhao, F. A Critical Review of Microelectrode Arrays and Strategies for Improving Neural Interfaces. *Adv. Healthc. Mater.* **8**, 1900558 (2019).
7. Lin, M. Z. & Schnitzer, M. J. Genetically encoded indicators of neuronal activity. *Nat. Neurosci.* **19**, 1142–1153 (2016).
8. Jin, L. *et al.* Single Action Potentials and Subthreshold Electrical Events Imaged in Neurons with a Fluorescent Protein Voltage Probe. *Neuron* **75**, 779–785 (2012).
9. Siegel, M. S. & Isacoff, E. Y. A Genetically Encoded Optical Probe of Membrane Voltage. *Neuron* **19**, 735–741 (1997).
10. Bando, Y., Sakamoto, M., Kim, S., Ayzenshtat, I. & Yuste, R. Comparative Evaluation of Genetically Encoded Voltage Indicators. *Cell Rep.* **26**, 802-813.e4 (2019).
11. Nakajima, R., Jung, A., Yoon, B.-J. & Baker, B. J. Optogenetic Monitoring of Synaptic Activity with Genetically Encoded Voltage Indicators. *Front. Synaptic Neurosci.* **8**, 22 (2016).
12. Yang, H. H. & St-Pierre, F. Genetically Encoded Voltage Indicators: Opportunities and Challenges. *J. Neurosci.* **36**, 9977–9989 (2016).
13. Chemla, S. *et al.* Improving voltage-sensitive dye imaging: with a little help from computational approaches. *Neurophotonics* **4**, 031215 (2017).

14. Habib, A. *et al.* Electro-plasmonic nanoantenna: A nonfluorescent optical probe for ultrasensitive label-free detection of electrophysiological signals. *Sci. Adv.* **5**, eaav9786 (2019).
15. Lebedev, M. A. & Nicolelis, M. A. L. Brain–machine interfaces: past, present and future. *Trends Neurosci.* **29**, 536–546 (2006).
16. Lebedev, M. A. & Nicolelis, M. A. L. Brain-Machine Interfaces: From Basic Science to Neuroprostheses and Neurorehabilitation. *Physiol. Rev.* **97**, 767–837 (2017).
17. Ramadan, R. A. & Vasilakos, A. V. Brain computer interface: control signals review. *Neurocomputing* **223**, 26–44 (2017).
18. Shih, J. J., Krusienski, D. J. & Wolpaw, J. R. Brain-Computer Interfaces in Medicine. *Mayo Clin. Proc.* **87**, 268–279 (2012).
19. Brambilla, C. *et al.* Combined Use of EMG and EEG Techniques for Neuromotor Assessment in Rehabilitative Applications: A Systematic Review. *Sensors* **21**, 7014 (2021).
20. Lozano, A. M. *et al.* Deep brain stimulation: current challenges and future directions. *Nat. Rev. Neurol.* **15**, 148–160 (2019).
21. Schwartz, A. B. Cortical neural prosthetics. *Annu. Rev. Neurosci.* **27**, 487–507 (2004).
22. Joshi-Imre, A. *et al.* Chronic recording and electrochemical performance of amorphous silicon carbide-coated Utah electrode arrays implanted in rat motor cortex. *J. Neural Eng.* **16**, 046006 (2019).
23. Chen, R., Canales, A. & Anikeeva, P. Neural Recording and Modulation Technologies. *Nat. Rev. Mater.* **2**, 16093 (2017).
24. Acarón Ledesma, H. *et al.* An atlas of nano-enabled neural interfaces. *Nat. Nanotechnol.* **14**, 645–657 (2019).
25. Ludwig, K. A. *et al.* Poly(3,4-ethylenedioxythiophene) (PEDOT) polymer coatings facilitate smaller neural recording electrodes. *J. Neural Eng.* **8**, 014001 (2011).
26. Urai, A. E., Doiron, B., Leifer, A. M. & Churchland, A. K. Large-scale neural recordings call for new insights to link brain and behavior. *Nat. Neurosci.* **25**, 11–19 (2022).

27. Demas, J. *et al.* High-speed, cortex-wide volumetric recording of neuroactivity at cellular resolution using light beads microscopy. *Nat. Methods* **18**, 1103–1111 (2021).
28. Fan, L. Z. *et al.* All-Optical Electrophysiology Reveals the Role of Lateral Inhibition in Sensory Processing in Cortical Layer 1. *Cell* **180**, 521-535.e18 (2020).
29. Kannan, M. *et al.* Fast, in vivo voltage imaging using a red fluorescent indicator. *Nat. Methods* **15**, 1108–1116 (2018).
30. Villette, V. *et al.* Ultrafast Two-Photon Imaging of a High-Gain Voltage Indicator in Awake Behaving Mice. *Cell* **179**, 1590-1608.e23 (2019).
31. Knöpfel, T. Genetically encoded optical indicators for the analysis of neuronal circuits. *Nat. Rev. Neurosci.* **13**, 687–700 (2012).
32. Kastrup, L. & Hell, S. W. Absolute Optical Cross Section of Individual Fluorescent Molecules. *Angew. Chem. Int. Ed.* **43**, 6646–6649 (2004).
33. Hochbaum, D. R. *et al.* All-optical electrophysiology in mammalian neurons using engineered microbial rhodopsins. *Nat. Methods* **11**, 825–833 (2014).
34. Scanziani, M. & Häusser, M. Electrophysiology in the age of light. *Nature* **461**, 930–939 (2009).
35. Cao, G. *et al.* Genetically Targeted Optical Electrophysiology in Intact Neural Circuits. *Cell* **154**, 904–913 (2013).
36. Efros, A. L. *et al.* Evaluating the potential of using quantum dots for monitoring electrical signals in neurons. *Nat. Nanotechnol.* **13**, 278–288 (2018).
37. Empedocles, S. A. & Bawendi, M. G. Quantum-Confined Stark Effect in Single CdSe Nanocrystallite Quantum Dots. *Science* **278**, 2114–2117 (1997).
38. Scholl, C. A. *et al.* Optical Noninvasive Brain–Computer Interface Development: Challenges and Opportunities. *Johns Hopkins APL Tech. Dig.* **35**, 8 (2021).
39. Carmena, J. M. Advances in Neuroprosthetic Learning and Control. *PLOS Biol.* **11**, e1001561 (2013).
40. Rabaey, J. M. Brain-machine interfaces as the new frontier in extreme miniaturization. in *2011 Proceedings of the European Solid-State Device Research Conference (ESSDERC)* 19–24 (2011). doi:10.1109/ESSDERC.2011.6044240.

41. Wu, N. *et al.* Electrode materials for brain–machine interface: A review. *InfoMat* **3**, 1174–1194 (2021).
42. Spira, M. E. & Hai, A. Multi-electrode array technologies for neuroscience and cardiology. *Nat. Nanotechnol.* **8**, 83–94 (2013).
43. Marx, V. Neurobiology: rethinking the electrode. *Nat. Methods* **11**, 1099–1103 (2014).
44. Nam, Y. & Wheeler, B. C. In Vitro Microelectrode Array Technology and Neural Recordings. *Crit. Rev. Biomed. Eng.* **39**, (2011).
45. Fernández, E. *et al.* Acute human brain responses to intracortical microelectrode arrays: challenges and future prospects. *Front. Neuroengineering* **7**, (2014).
46. Johnson, L. J. *et al.* A novel high electrode count spike recording array using an 81,920 pixel transimpedance amplifier-based imaging chip. *J. Neurosci. Methods* **205**, 223–232 (2012).
47. Jun, J. J. *et al.* Fully integrated silicon probes for high-density recording of neural activity. *Nature* **551**, 232–236 (2017).
48. Canales, A. *et al.* Multifunctional fibers for simultaneous optical, electrical and chemical interrogation of neural circuits in vivo. *Nat. Biotechnol.* **33**, 277–284 (2015).
49. Alivisatos, A. P. *et al.* Nanotools for Neuroscience and Brain Activity Mapping. *ACS Nano* **7**, 1850–1866 (2013).
50. Musk, E. & Neuralink. An Integrated Brain-Machine Interface Platform With Thousands of Channels. *J. Med. Internet Res.* **21**, e16194 (2019).
51. Kelly, R. C. *et al.* Comparison of recordings from microelectrode arrays and single electrodes in the visual cortex. *J. Neurosci.* **27**, 261–264 (2007).
52. Neely, R. M., Piech, D. K., Santacruz, S. R., Maharbiz, M. M. & Carmena, J. M. Recent advances in neural dust: towards a neural interface platform. *Curr. Opin. Neurobiol.* **50**, 64–71 (2018).
53. Seo, D. *et al.* Wireless Recording in the Peripheral Nervous System with Ultrasonic Neural Dust. *Neuron* **91**, 529–539 (2016).
54. Seo, D., Carmena, J. M., Rabaey, J. M., Alon, E. & Maharbiz, M. M. Neural Dust: An Ultrasonic, Low Power Solution for Chronic Brain-Machine Interfaces. Preprint at <https://doi.org/10.48550/arXiv.1307.2196> (2013).

55. Patch, K. Neural dust swept up in latest leap for bioelectronic medicine. *Nat. Biotechnol.* **39**, 255–256 (2021).
56. Adam, Y. *et al.* Voltage imaging and optogenetics reveal behaviour-dependent changes in hippocampal dynamics. *Nature* **569**, 413–417 (2019).
57. Vogt, N. Voltage imaging in vivo. *Nat. Methods* **16**, 573–573 (2019).
58. Rivnay, J., Wang, H., Fenno, L., Deisseroth, K. & Malliaras, G. G. Next-generation probes, particles, and proteins for neural interfacing. *Sci. Adv.* **3**, e1601649 (2017).
59. Kralj, J. M., Douglass, A. D., Hochbaum, D. R., Maclaurin, D. & Cohen, A. E. Optical recording of action potentials in mammalian neurons using a microbial rhodopsin. *Nat. Methods* **9**, 90–95 (2012).
60. Flytzanis, N. C. *et al.* Archaelhodopsin variants with enhanced voltage-sensitive fluorescence in mammalian and *Caenorhabditis elegans* neurons. *Nat. Commun.* **5**, 4894 (2014).
61. Resendez, S. L. *et al.* Visualization of cortical, subcortical, and deep brain neural circuit dynamics during naturalistic mammalian behavior with head-mounted microscopes and chronically implanted lenses. *Nat. Protoc.* **11**, 566–597 (2016).
62. De La Crompe, B., Coulon, P. & Diester, I. Functional interrogation of neural circuits with virally transmitted optogenetic tools. *J. Neurosci. Methods* **345**, 108905 (2020).
63. Daigle, T. L. *et al.* A Suite of Transgenic Driver and Reporter Mouse Lines with Enhanced Brain-Cell-Type Targeting and Functionality. *Cell* **174**, 465-480.e22 (2018).
64. Marshall, J. D. & Schnitzer, M. J. Optical Strategies for Sensing Neuronal Voltage Using Quantum Dots and Other Semiconductor Nanocrystals. *ACS Nano* **7**, 4601–4609 (2013).
65. Nag, O. K. *et al.* Quantum Dot–Peptide–Fullerene Bioconjugates for Visualization of in Vitro and in Vivo Cellular Membrane Potential. *ACS Nano* **11**, 5598–5613 (2017).
66. Walters, G. *et al.* The quantum-confined Stark effect in layered hybrid perovskites mediated by orientational polarizability of confined dipoles. *Nat. Commun.* **9**, 4214 (2018).

67. Anker, J. N. *et al.* Biosensing with plasmonic nanosensors. *Nat. Mater.* **7**, 442–453 (2008).
68. Au, B. W.-C. & Chan, K.-Y. Towards an All-Solid-State Electrochromic Device: A Review of Solid-State Electrolytes and the Way Forward. *Polymers* **14**, 2458 (2022).
69. Engheta, N. Circuits with Light at Nanoscales: Optical Nanocircuits Inspired by Metamaterials. *Science* **317**, 1698–1702 (2007).
70. Alù, A. & Engheta, N. Tuning the scattering response of optical nanoantennas with nanocircuit loads. *Nat. Photonics* **2**, 307–310 (2008).
71. Alfonso, F. S. *et al.* Label-free optical detection of bioelectric potentials using electrochromic thin films. *Proc. Natl. Acad. Sci. U. S. A.* **117**, 17260–17268 (2020).
72. Campbell, A. & Wu, C. Chronically Implanted Intracranial Electrodes: Tissue Reaction and Electrical Changes. *Micromachines* **9**, 430 (2018).
73. Shi, L., Sordillo, L. A., Rodríguez-Contreras, A. & Alfano, R. Transmission in near-infrared optical windows for deep brain imaging. *J. Biophotonics* **9**, 38–43 (2016).
74. Shin, J., Müller, K.-R. & Hwang, H.-J. Near-infrared spectroscopy (NIRS)-based eyes-closed brain-computer interface (BCI) using prefrontal cortex activation due to mental arithmetic. *Sci. Rep.* **6**, 36203 (2016).
75. Nemani, A. *et al.* Assessing bimanual motor skills with optical neuroimaging. *Sci. Adv.* **4**, eaat3807 (2018).
76. Rahman, Md. A., Siddik, A. B., Ghosh, T. K., Khanam, F. & Ahmad, M. A Narrative Review on Clinical Applications of fNIRS. *J. Digit. Imaging* **33**, 1167–1184 (2020).
77. Cortese, L. *et al.* Performance Assessment of a Commercial Continuous-Wave Near-Infrared Spectroscopy Tissue Oximeter for Suitability for Use in an International, Multi-Center Clinical Trial. *Sensors* **21**, 6957 (2021).
78. Yamada, Y., Suzuki, H. & Yamashita, Y. Time-Domain Near-Infrared Spectroscopy and Imaging: A Review. *Appl. Sci.* **9**, 1127 (2019).
79. Torricelli, A. *et al.* Time domain functional NIRS imaging for human brain mapping. *NeuroImage* **85**, 28–50 (2014).

80. Herold, F., Wiegel, P., Scholkmann, F. & Müller, N. G. Applications of Functional Near-Infrared Spectroscopy (fNIRS) Neuroimaging in Exercise–Cognition Science: A Systematic, Methodology-Focused Review. *J. Clin. Med.* **7**, 466 (2018).
81. Baker, W. B. *et al.* Modified Beer-Lambert law for blood flow. *Biomed. Opt. Express* **5**, 4053–4075 (2014).
82. Ban, H. Y. *et al.* Kernel Flow: a high channel count scalable time-domain functional near-infrared spectroscopy system. *J. Biomed. Opt.* **27**, (2022).
83. Huang, J., Zhang, J., Zhang, T., Wang, P. & Zheng, Z. Increased Prefrontal Activation During Verbal Fluency Task After Repetitive Transcranial Magnetic Stimulation Treatment in Depression: A Functional Near-Infrared Spectroscopy Study. *Front. Psychiatry* **13**, (2022).
84. Li, L. *et al.* Whole-cortical graphical networks at wakeful rest in young and older adults revealed by functional near-infrared spectroscopy. *Neurophotonics* **5**, 035004 (2018).
85. Erickson, H. P. Size and Shape of Protein Molecules at the Nanometer Level Determined by Sedimentation, Gel Filtration, and Electron Microscopy. *Biol. Proced. Online* **11**, 32–51 (2009).
86. Chen, W.-L. *et al.* Functional Near-Infrared Spectroscopy and Its Clinical Application in the Field of Neuroscience: Advances and Future Directions. *Front. Neurosci.* **14**, (2020).
87. Glover, G. H. Overview of Functional Magnetic Resonance Imaging. *Neurosurg. Clin. N. Am.* **22**, 133–139 (2011).
88. Buxton, R. B. The physics of functional magnetic resonance imaging (fMRI). *Rep. Prog. Phys. Phys. Soc. G. B.* **76**, 096601 (2013).
89. Rohlf, J. W. *Modern Physics from alpha to Z0*. (Wiley, 1994).
90. Gore, J. C. Principles and practice of functional MRI of the human brain. *J. Clin. Invest.* **112**, 4–9 (2003).
91. Logothetis, N. K. What we can do and what we cannot do with fMRI. *Nature* **453**, 869–878 (2008).
92. Song, A. W., Guo, H. & Truong, T.-K. Single-shot ADC imaging for fMRI. *Magn. Reson. Med.* **57**, 417–422 (2007).

93. Stehling, M. K., Turner, R. & Mansfield, P. Echo-Planar Imaging: Magnetic Resonance Imaging in a Fraction of a Second. *Science* **254**, 43–50 (1991).
94. Buxton, R. B. *Introduction to Functional Magnetic Resonance Imaging: Principles and Techniques*. (Cambridge University Press, 2009).
95. Feinberg, D. A. *et al.* Multiplexed Echo Planar Imaging for Sub-Second Whole Brain fMRI and Fast Diffusion Imaging. *PLoS ONE* **5**, e15710 (2010).
96. Turner, R. Uses, misuses, new uses and fundamental limitations of magnetic resonance imaging in cognitive science. *Philos. Trans. R. Soc. B Biol. Sci.* **371**, 20150349 (2016).
97. Buxton, R. B. Interpreting Oxygenation-Based Neuroimaging Signals: The Importance and the Challenge of Understanding Brain Oxygen Metabolism. *Front. Neuroenergetics* **2**, 8 (2010).
98. Lu, H., Golay, X., Pekar, J. J. & Van Zijl, P. C. M. Functional magnetic resonance imaging based on changes in vascular space occupancy. *Magn. Reson. Med.* **50**, 263–274 (2003).
99. Moeller, S. *et al.* Multiband Multislice GE-EPI at 7 Tesla, With 16-Fold Acceleration Using Partial Parallel Imaging With Application to High Spatial and Temporal Whole-Brain fMRI. *Magn. Reson. Med. Off. J. Soc. Magn. Reson. Med. Soc. Magn. Reson. Med.* **63**, 1144–1153 (2010).
100. Van Essen, D. C. *et al.* The Human Connectome Project: A data acquisition perspective. *NeuroImage* **62**, 2222–2231 (2012).
101. Alivisatos, A. P. *et al.* The Brain Activity Map. *Science* **339**, 1284–1285 (2013).
102. Shroff, S. N. *et al.* Voltage Imaging of Cardiac Cells and Tissue Using the Genetically Encoded Voltage Sensor Archon1. *iScience* **23**, 100974 (2020).
103. Wightman, R. M. Probing Cellular Chemistry in Biological Systems with Microelectrodes. *Science* **311**, 1570–1574 (2006).
104. Yuan, X. *et al.* Versatile live-cell activity analysis platform for characterization of neuronal dynamics at single-cell and network level. *Nat. Commun.* **11**, 4854 (2020).
105. Tsai, D., Sawyer, D., Bradd, A., Yuste, R. & Shepard, K. L. A very large-scale microelectrode array for cellular-resolution electrophysiology. *Nat. Commun.* **8**, 1802 (2017).

106. Ebbesen, T. W., Lezec, H. J., Ghaemi, H. F., Thio, T. & Wolff, P. A. Extraordinary optical transmission through sub-wavelength hole arrays. *Nature* **391**, 667–669 (1998).
107. Nalwa, H. S. *Handbook of Advanced Electronic and Photonic Materials and Devices, Ten-Volume Set*. (Academic Press, 2000).
108. Palik, E. D. *Handbook of Optical Constants of Solids*. (Academic Press, 1998).
109. Baba, A., Lübber, J., Tamada, K. & Knoll, W. Optical Properties of Ultrathin Poly(3,4-ethylenedioxythiophene) Films at Several Doping Levels Studied by In Situ Electrochemical Surface Plasmon Resonance Spectroscopy. *Langmuir* **19**, 9058–9064 (2003).
110. Jiang, J. *et al.* Plasmonic nano-arrays for ultrasensitive bio-sensing. *Nanophotonics* **7**, 1517–1531 (2018).
111. Jain, V., Yochum, H. M., Montazami, R. & Heflin, J. R. Millisecond switching in solid state electrochromic polymer devices fabricated from ionic self-assembled multilayers. *Appl. Phys. Lett.* **92**, 033304 (2008).
112. Can, U. I., Nagarajan, N., Vural, D. C. & Zorlutuna, P. Muscle-Cell-Based “Living Diodes”. *Adv. Biosyst.* **1**, 1600035 (2017).
113. Jaimes, R. *et al.* Lights, camera, path splitter: a new approach for truly simultaneous dual optical mapping of the heart with a single camera. *BMC Biomed. Eng.* **1**, 25 (2019).
114. Fu, J., Gao, J., Pi, R. & Liu, P. An Optimized Protocol for Culture of Cardiomyocyte from Neonatal Rat. *Cytotechnology* **49**, 109–116 (2005).
115. Hardy, N., Habib, A., Ivanov, T. & Yanik, A. A. Neuro-SWARM³: System-on-a-Nanoparticle for Wireless Recording of Brain Activity. *IEEE Photonics Technol. Lett.* **33**, 900–903 (2021).
116. Asplund, M. *et al.* Toxicity evaluation of PEDOT/biomolecular composites intended for neural communication electrodes. *Biomed. Mater.* **4**, 045009 (2009).
117. Posadas, I., Monteagudo, S. & Ceña, V. Nanoparticles for brain-specific drug and genetic material delivery, imaging and diagnosis. *Nanomed.* **11**, 833–849 (2016).

118. Joye, N., Schmid, A. & Leblebici, Y. Electrical modeling of the cell–electrode interface for recording neural activity from high-density microelectrode arrays. *Neurocomputing* **73**, 250–259 (2009).
119. Caglar, M. *et al.* All-Optical Detection of Neuronal Membrane Depolarization in Live Cells Using Colloidal Quantum Dots. *Nano Lett.* **19**, 8539–8549 (2019).
120. Wan, H. *et al.* A bright organic NIR-II nanofluorophore for three-dimensional imaging into biological tissues. *Nat. Commun.* **9**, 1171 (2018).
121. Ladutenko, K., Pal, U., Rivera, A. & Peña-Rodríguez, O. Mie calculation of electromagnetic near-field for a multilayered sphere. *Comput. Phys. Commun.* **214**, 225–230 (2017).
122. Peña, O. & Pal, U. Scattering of electromagnetic radiation by a multilayered sphere. *Comput. Phys. Commun.* **180**, 2348–2354 (2009).
123. Mun, J., So, S. & Rho, J. Spectrally Sharp Plasmon Resonances in the Near Infrared: Subwavelength Core-shell Nanoparticles. *Phys. Rev. Appl.* **12**, 044072 (2019).
124. Chang, S. H., Chiang, C.-H., Kao, F.-S., Tien, C.-L. & Wu, C.-G. Unraveling the Enhanced Electrical Conductivity of PEDOT:PSS Thin Films for ITO-Free Organic Photovoltaics. *IEEE Photonics J.* **6**, 1–7 (2014).
125. Kittel, C. *Introduction to solid state physics.* (Wiley, 2005).
126. Griffiths, D. J. *Introduction to electrodynamics.* (Pearson, 2013).
127. Du, Y. *et al.* Dielectric Properties of DMSO-Doped-PEDOT:PSS at THz Frequencies. *Phys. Status Solidi B* **255**, 1700547 (2018).
128. Yamashita, M., Otani, C., Okuzaki, H. & Shimizu, M. Nondestructive measurement of carrier mobility in conductive polymer PEDOT:PSS using Terahertz and infrared spectroscopy. in *2011 XXXth URSI General Assembly and Scientific Symposium* 1–4 (IEEE, 2011). doi:10.1109/URSIGASS.2011.6050616.
129. Oheim, M., Beaupaire, E., Chaigneau, E., Mertz, J. & Charpak, S. Two-photon microscopy in brain tissue: parameters influencing the imaging depth. *J. Neurosci. Methods* **111**, 29–37 (2001).
130. Izhikevich, E. M. Simple model of spiking neurons. *IEEE Trans. Neural Netw.* **14**, 1569–1572 (2003).

131. Rowland, C. E. *et al.* Electric Field Modulation of Semiconductor Quantum Dot Photoluminescence: Insights Into the Design of Robust Voltage-Sensitive Cellular Imaging Probes. *Nano Lett.* **15**, 6848–6854 (2015).
132. Chen, R., Romero, G., Christiansen, M. G., Mohr, A. & Anikeeva, P. Wireless magnetothermal deep brain stimulation. *Science* **347**, 1477–1480 (2015).
133. Lee, J. *et al.* Non-contact long-range magnetic stimulation of mechanosensitive ion channels in freely moving animals. *Nat. Mater.* **20**, 1029–1036 (2021).
134. Westrum, E. F. & Grønvold, F. Magnetite (Fe₃O₄) Heat capacity and thermodynamic properties from 5 to 350 K, low-temperature transition. *J. Chem. Thermodyn.* **1**, 543–557 (1969).
135. Liu, J. *et al.* Thermal Conductivity and Elastic Constants of PEDOT:PSS with High Electrical Conductivity. *Macromolecules* **48**, 585–591 (2015).
136. Takahashi, Y. & Akiyama, H. Heat capacity of gold from 80 to 1000 K. *Thermochim. Acta* **109**, 105–109 (1986).
137. DeArmitt, C. Magnetite. in *Polymers and Polymeric Composites: A Reference Series* (ed. Palsule, S.) 1–13 (Springer Berlin Heidelberg, 2016). doi:10.1007/978-3-642-37179-0_34-2.
138. Young, H. D. *University physics*. (Addison-Wesley Pub. Co., 1992).
139. Bubnova, O. *et al.* Optimization of the thermoelectric figure of merit in the conducting polymer poly(3,4-ethylenedioxythiophene). *Nat. Mater.* **10**, 429–433 (2011).
140. Monteith, J. L. & Unsworth, M. H. *Principles of environmental physics: plants, animals, and the atmosphere*. (Elsevier/Academic Press, 2013).
141. Query, M. R. *Optical Constants*. <https://apps.dtic.mil/sti/citations/ADA158623> (1985).
142. National Academies of Sciences, E., Division, H. and M., Policy, B. on H. S. & Disorders, F. on N. and N. S. *Traversing the Blood–Brain Barrier: Challenges and Opportunities. Enabling Novel Treatments for Nervous System Disorders by Improving Methods for Traversing the Blood–Brain Barrier: Proceedings of a Workshop* (National Academies Press (US), 2018).
143. Zhao, Z., Nelson, A. R., Betsholtz, C. & Zlokovic, B. V. Establishment and Dysfunction of the Blood-Brain Barrier. *Cell* **163**, 1064–1078 (2015).

144. Abbott, N. J., Rönnbäck, L. & Hansson, E. Astrocyte–endothelial interactions at the blood–brain barrier. *Nat. Rev. Neurosci.* **7**, 41–53 (2006).
145. Lombardo, S. M., Schneider, M., Türelı, A. E. & Günday Türelı, N. Key for crossing the BBB with nanoparticles: the rational design. *Beilstein J. Nanotechnol.* **11**, 866–883 (2020).
146. Teleanu, D. M., Chircov, C., Grumezescu, A. M. & Teleanu, R. I. Neuronanomedicine: An Up-to-Date Overview. *Pharmaceutics* **11**, (2019).
147. Michaelis, K. *et al.* Covalent Linkage of Apolipoprotein E to Albumin Nanoparticles Strongly Enhances Drug Transport into the Brain. *J. Pharmacol. Exp. Ther.* **317**, 1246–1253 (2006).
148. Fortuni, B. *et al.* Polymeric Engineering of Nanoparticles for Highly Efficient Multifunctional Drug Delivery Systems. *Sci. Rep.* **9**, 2666 (2019).
149. Sur, S. *et al.* Recent developments in functionalized polymer nanoparticles for efficient drug delivery system. *Nano-Struct. Nano-Objects* **20**, 100397 (2019).
150. Ramaswamy, B. *et al.* Movement of Magnetic Nanoparticles in Brain Tissue: Mechanisms and Safety. *Nanomedicine Nanotechnol. Biol. Med.* **11**, 1821–1829 (2015).
151. Thomsen, L. B. *et al.* Uptake and Transport of Superparamagnetic Iron Oxide Nanoparticles through Human Brain Capillary Endothelial Cells. *ACS Chem. Neurosci.* **4**, 1352–1360 (2013).
152. Carezza, E. *et al.* In vitro angiogenic performance and in vivo brain targeting of magnetized endothelial progenitor cells for neurorepair therapies. *Nanomedicine Nanotechnol. Biol. Med.* **10**, 225–234 (2014).
153. Lu, W., Jiang, N. & Wang, J. Active Electrochemical Plasmonic Switching on Polyaniline-Coated Gold Nanocrystals. *Adv. Mater.* **29**, 1604862 (2017).
154. Peng, J. *et al.* Scalable electrochromic nanopixels using plasmonics. *Sci. Adv.* **5**, eaaw2205 (2019).
155. Kang, J.-H., Oh, Y.-J., Paek, S.-M., Hwang, S.-J. & Choy, J.-H. Electrochromic device of PEDOT–PANI hybrid system for fast response and high optical contrast. *Sol. Energy Mater. Sol. Cells* **93**, 2040–2044 (2009).
156. Brinson, B. E. *et al.* Nanoshells Made Easy: Improving Au Layer Growth on Nanoparticle Surfaces. *Langmuir* **24**, 14166–14171 (2008).

157. Dong, Y. Z., Choi, K., Kwon, S. H., Nam, J.-D. & Choi, H. J. Nanoparticles Functionalized by Conducting Polymers and Their Electrorheological and Magnetorheological Applications. *Polymers* **12**, (2020).
158. Sulaymon, A. H. & Abbar, A. H. *Scale-Up of Electrochemical Reactors. Electrolysis* (IntechOpen, 2012). doi:10.5772/48728.
159. Kelley, D. H. Brain cerebrospinal fluid flow. *Phys. Rev. Fluids* **6**, 070501 (2021).
160. Lesniak, A. *et al.* Nanoparticle Adhesion to the Cell Membrane and Its Effect on Nanoparticle Uptake Efficiency. *J. Am. Chem. Soc.* **135**, 1438–1444 (2013).
161. Prodan, E. & Nordlander, P. Plasmon hybridization in spherical nanoparticles. *J. Chem. Phys.* **120**, 5444–5454 (2004).
162. He, H. *et al.* Biocompatible Conductive Polymers with High Conductivity and High Stretchability. *ACS Appl. Mater. Interfaces* **11**, 26185–26193 (2019).
163. Miriani, R. M., Abidian, M. R. & Kipke, D. R. Cytotoxic analysis of the conducting polymer PEDOT using myocytes. *Annu. Int. Conf. IEEE Eng. Med. Biol. Soc. IEEE Eng. Med. Biol. Soc. Annu. Int. Conf.* **2008**, 1841–1844 (2008).
164. Goodman, A. M. *et al.* The Surprising in Vivo Instability of Near-IR-Absorbing Hollow Au–Ag Nanoshells. *ACS Nano* **8**, 3222–3231 (2014).
165. Pranti, A. S., Schander, A., Bödecker, A. & Lang, W. PEDOT: PSS coating on gold microelectrodes with excellent stability and high charge injection capacity for chronic neural interfaces. *Sens. Actuators B Chem.* **275**, 382–393 (2018).
166. Malhotra, N. *et al.* Potential Toxicity of Iron Oxide Magnetic Nanoparticles: A Review. *Molecules* **25**, 3159 (2020).
167. Guerrini, L., Alvarez-Puebla, R. A. & Pazos-Perez, N. Surface Modifications of Nanoparticles for Stability in Biological Fluids. *Mater. Basel Switz.* **11**, E1154 (2018).